Master's thesis

NTNU
Norwegian University of Science and Technology
Faculty of Engineering
Department of Structural Engineering

Fjelldal, Jens Roar
Kjøle, Agnethe Maria

Damage Identification of Structures with Accelerometers Under Idealized Conditions

Master's thesis in Civil and Environmental Engineering
Supervisor: Gunnstein T. Frøseth
June 2020

NTNU
Kunnskap for en bedre verden

Fjelldal, Jens Roar
Kjøle, Agnethe Maria

Damage Identification of Structures with Accelerometers Under Idealized Conditions

Master's thesis in Civil and Environmental Engineering
Supervisor: Gunnstein T. Frøseth
June 2020

Norwegian University of Science and Technology
Faculty of Engineering
Department of Structural Engineering

NTNU

Kunnskap for en bedre verden

Preface

The research presented in this thesis was conducted by the Department of Structural Engineering of the Norwegian University of Science and Technology (NTNU), under the supervision of Associate Professor Gunnstein Thomas Frøseth and PhD Candidate Bjørn Thomas Svendsen. We thankfully acknowledge the assistance and encouragement from supervisors. Gunnstein T. Frøseth deserves some extra kudos as he performed all experiments.

Trondheim, June 2020 J. R. Fjelldal & A. M. Kjøle

Abstract

Today, many existing structures, such as bridges, aircrafts, offshore oil platforms and buildings, are reaching the end of their original design life. It is not economical to replace these systems. Damage detection techniques are therefore a research of interest, in order to develop and implement techniques that allow structures to work safely, even if their service life has been reached. This thesis uses different damage sensitive features to identify three damages introduced in a cantilever beam: point masses, boundary damages and cuts. First, a numerical study was performed in order to establish a sufficient sensor layout for experimental testing. A finite element model was created, before a numerical damage identification study was performed. Based on the results and assumptions made from the numerical study, an experimental study was performed. The damage sensitive features evaluated were Natural Frequency Shifts, Mode Shapes, Mode Shape Curvature, Modal Flexibility and Statistical Moments. The thesis revolves around the difficulties in which damage scenarios that can be identified by the use of acceleration measurements, how large the damages has to be in order to be detected, and whether it is possible to identify the severity of the damage. The thesis also discuss how the results can be implemented in full scale monitoring of real-life structures.

The results show that for a low number of sensors, with unequal spacing, damage identification can be difficult. Most point mass and boundary damages were identified from the recorded response histories, while cut damages had to be severe in order to get good results. Further, the results show that damage identification is possible by the use of the simplest techniques: Natural Frequency Shifts, Mode Shapes, and Modal Flexibility. These damage sensitive features identify and classify the point mass, boundary and cut damages. None of the evaluated features managed to locate damages. The proposed damage features can contribute to the identification of structural damage, as it proves that the simplest methods obtain better result for damage identification.

Sammendrag

Dagens vei og jernbanenett består av et stort antall bruer som enten nærmer seg eller har overskredet levetiden som ble lagt til grunn for dimensjonering av disse konstruksjonene. Det er ikke økonomisk å erstatte disse systemene fullstendig. Det er derfor stor interesse for å utvikle og implementere deteksjonsteknikker av skader, slik at konstruksjoner kan fortsette å fungere trygt selv om levetiden deres er nådd. Denne oppgaven utforsker forskjellige skade-features for å identifisere tre skader: punktmasser, skader på opplager og kutt.

En numerisk studie ble først utført for å utforme optimal sensor plassering for eksperimentell testing. En numerisk modell ble etablert før en numerisk skadeidentifikasjon ble utført. En eksperimentell studie ble deretter utført basert på resultatene og antagelsene gjort fra den numeriske studien. Skademetodene som ble evaluert var egenfrekvenser ("Natural Frequency Shifts"), modeformer ("Mode Shapes"), kurvatur ("Mode Shape Curvature"), fleksibilitet ("Modal Flexibility") og statistiske momenter. Oppgaven dreier seg om identifisering av skadescenarioer ved bruk av akselerasjonsmålinger, hvor store skader må være for å bli oppdaget, og om det er mulig å identifisere skadens alvorlighetsgrad. Avhandlingen drøfter også hvordan resultatene kan implementeres i fullskala overvåking av eksisterende konstruksjoner.

Resultatene viser at skadeidentifikasjon kan være vanskelig for et lavt antall sensorer, med ujevn avstand. De fleste punktmasse- og grense-skader ble identifisert, men kuttene krevde store magnituder/dybder for å oppnå gode resultater. Videre, viser resultatene at skadeidentifisering er mulig ved bruk av de enkleste teknikkene basert på egenfrekvens, modeformer, og fleksibilitet. De foreslåtte skademetodene kan forbedre skadeidentifisering av eksisterende konstruksjoner, da det viser seg at de enkle metodene oppnår bedre resultat for identifisering.

Contents

Chapter 1

Introduction

Today, the road and railway network consists of a large number of bridges that are either near the end of, or have already exceeded their original design life, which was the basis of the dimensioning. Technological development, population growth and global warming have led to a significant increase in the load on the bridges. Larger axle loads, larger traffic volumes, more extreme wind, wave and snow loads are affecting the load carrying capacity of these bridges [8]. Additionally, larger structures will be wanted in areas of more exposed environments, such as offshore wind turbines, bridges on high-speed railway networks and fjord crossings, requiring larger utilization of the structures than what can be seen today. Ageing infrastructure, higher loads and the need of structures in areas with extreme environments increases the probability of damages and fractures in critical infrastructure.

Structural health monitoring is a technology which uses continuous measures, together with advanced signal processing techniques, to identify and warn of damages in structures, so that necessary rehabilitating and maintenance measures can be implemented. By monitoring structures, expensive inspection programs can be replaced by inaccessible structural elements. Today this is carried out by special-

Figure 1.1: Damaged joint (Photo: Gunnstein T. Frøseth).

ized personnel, working in dangerous environments at frequent intervals. Thus, structural monitoring can contribute to proper use and optimal maintenance of critical infrastructure. This have resulted in the desire to analyse and detect possible damages at the structure in an easy and cost efficient way without stopping the daily use of the structures.

In this thesis, damage identification of a cantilever beam has been studied numerically and experimentally. Three different damages have been evaluated: boundary damages, point mass damages and cut damages. The boundary damages, represented as removed bolts, are severe damages and also a quite common damage scenario. Damages on the boundary conditions can be a result of fatigue, wear and overloads. A point mass is usually easy to detect visually, but is included in this thesis due to a lack of test pieces. The stiffness cannot be directly reduced several times, as these type of damages are hard to reverse. Cuts are such stiffness reducing damages, and are not always easy to detect by visual inspections. Typical damages represented by cuts are corrosion, actual cuts or other local material damages, such as fatigue, in an element. This thesis investigates different methods and features for damage identification based on acceleration measurements. The goal is to determine which damages that can be identified by means of acceleration measurements, how large the damage must be before it can be identified, and whether the severity of identified damages can be determined from the measurement data.

The thesis is divided into 5 chapters and an appendix. A short presentation of the chapters are given below.

Chapter 2: An introduction to the theory relevant for the work performed for this thesis. The chapter includes theory of structural dynamics, Rayleigh damping, modal analysis, structural health monitoring and damage identification.

Chapter 3: The case study of the cantilever beam is presented. The experimental setup and the system identification of the cantilever beam is presented, as well as the Finite Element model constructed. Natural frequencies and modal shapes of the experimental and numerical case studies are established. The chapter also includes the numerical and experimental implementation of damages evaluated in the thesis.

Chapter 4: The results of the experimental case study is presented and discussed. The strength of different damage features are discusses based on the results.

Chapter 5: Conclusion based on the results of the previous chapters are presented.

Appendix A: Relevant tables.

Chapter 2

Theory

Section 2.1 to 2.5 were written by the students during the fall of 2019, as a part of projects in *TKT4520 - Structural Dynamics* [7, 12].

2.1 Multi Degree of Freedom Systems

Structures are complex models and must be modelled as multi-degree of freedom systems. The equations of motion of a multi-degree of freedom system subjected to external forces can be written on matrix form as

$$[M]\{\ddot{u}\} + [C]\{\dot{u}\} + [K]\{u\} = \{P(t)\}, \tag{2.1}$$

where $[M]$ is the mass matrix, $[C]$ is the damping matrix, $[K]$ is the stiffness matrix and $\{P(t)\}$ is the vector containing the applied forces. For complex structural systems, with a large number of degrees of freedom (DOFs), the equation of motion will be very difficult to solve. These cases are often solved by performing a finite element analysis. For structural systems with fewer degrees of freedom, the mass, damping and stiffness matrices can be established, and the equation of motion can be solved with the often used approach of modal analysis. The modal analysis assumes a solution to the equation of motion in (2.1) on the form

$$\{u(x,t)\} = \sum_{n=1}^{N} \{\phi_n(x)\} q_n(t) = [\Phi]\{q(t)\}, \tag{2.2}$$

where ϕ_n is the modal shape of a generic solution with natural frequency ω_n, and $q_n(t)$ is a simple harmonic function dependent of time. The assumed solution is a linear combination, where the modal shape represents the physical deformation of a structure, when being excited by a dynamic force with the same frequency as the natural frequency of the structure itself. The modal shape is a dimensionless parameter, and therefore freely scalable. Figure 2.1 shows the first 5 theoretical modes of a cantilever beam. These are important when evaluating the dynamic response of a civil structure, as they indicate how a structure will behave at resonance frequency.

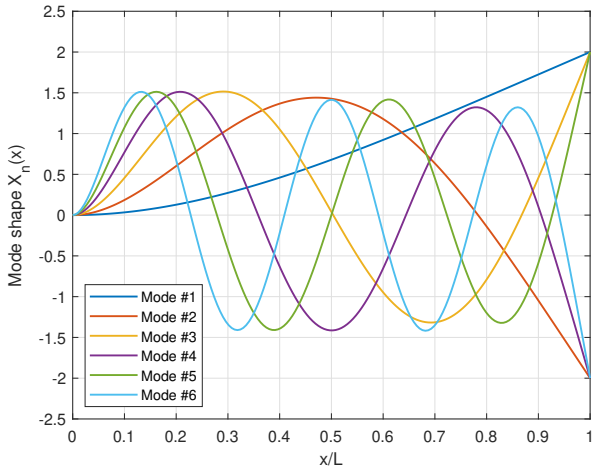

Figure 2.1: Natural modal shapes of cantilever beam

2.2 Estimation of Rayleigh Damping coefficients

This section presents a proposed approach to approximate Rayleigh Damping coefficients [3]. Damping is an important characteristic in dynamic analysis of structures. Damping values are treated as Rayleigh Damping in the form of

$$[C] = \alpha[M] + \beta[K], \tag{2.3}$$

where [C] is the damping matrix of the system, and α and β are pre-defined constants. When introducing Rayleigh damping to a model, an estimation of the Rayleigh damping coefficient must be made. The modal transformation of the damping matrix [C] above, result in:

$$2\zeta_i\omega_i = \alpha + \beta\omega_i^2, \tag{2.4}$$

which can be simplified to the following expression for the damping ratio:

$$\zeta_i = \frac{\alpha}{2\omega_i} + \frac{\beta\omega_i}{2}. \tag{2.5}$$

Equation (2.5) shows that the damping ratio is proportional to the natural frequencies of the structure.

When evaluating structures with a large number of DOFs, difficulties arise when obtaining meaningful values of the damping coefficients. For large structures, only a certain amount of modes, those contributing to the dynamic behavior, are relevant. The number of significant modes are decided from the the mass participation factors. The modes that make up 95% of the total mass, are included in the calculation of the Rayleigh damping coefficients [3].

The Rayleigh damping coefficients are calculated based on three sets of data. The results are compared to a linear interpolation, where the coefficients from the approach that best fits the interpolation is chosen.

In the first data set, an initial damping ratio ζ_1 for the first mode of the system, and a damping ratio ζ_m for the m^{th} significant mode, are selected. The intermediate modes i are obtained through linear interpolation:

$$\zeta_i = \frac{\zeta_m - \zeta_1}{\omega_m - \omega_1}(\omega_i - \omega_1) + \zeta_1, \qquad i \leq m \tag{2.6}$$

where ζ_i is the damping ratio of the i^{th} mode. Then the damping coefficient β is calculated based on the 1^{st} and m^{th} fundamental frequencies (ω_1 and ω_m) as:

$$\beta = \frac{2\zeta_1\omega_1 - 2\zeta_m\omega_m}{\omega_1^2 - \omega_m^2}. \tag{2.7}$$

The value of β is substituted back into equation (2.4) to obtain a value for α. The second data set consists of ζ_1, $\zeta_{2.5m}$, ω_1 and $\omega_{2.5m}$. The intermediate modes greater than m are extrapolated based on the following expression:

$$\zeta_i = \frac{\zeta_m - \zeta_1}{\omega_m - \omega_1}(\omega_{i+1} - \omega_m) + \zeta_1, \qquad m < i \leq 2.5m \tag{2.8}$$

The Rayleigh damping coefficients are calculated by equation (2.4) and (2.7). The third data set is calculated based on the averages of the first and second data sets. The three different results are plotted against a linear interpolation calculated from equation (2.5).

2.3 System Identification

By evaluating the dynamic response of the system, important information about the system behavior can be revealed. Experimental tests have become a common tool to use in order to gain knowledge about the dynamic response of civil structures. Experimental identification of modal parameters, such as natural frequencies ω_n, damping ratios ζ_n and modal shapes ϕ_n, date back to the middle of the 20th century [17]. By assuming modal expansion as in equation (2.2), the dynamic behavior can be described by a linear combination of natural modes. Each mode has its own characteristic set of parameters that depend on the geometry of the structure, material properties and boundary conditions. These modal characteristics can be identified from measurements obtained from experimental or operational modal analysis.

Experimental Modal Analysis (EMA) is an analysis method where the system of evaluation is subjected to a known vibration (input), and the vibration response (input) of the structure is measured. The application of EMA on civil structures can be challenging, due to the fact that structures can be of large dimensions, and have a low frequency range, Therefore, the application of controlled and measurable excitation requires heavy and expensive devices to induce sufficient level of

excitation [17]. This has led to an increased focus on Operational Modal Analysis (OMA), where the experimental estimation is reliant on ambient excitation from the environment. The modal parameters obtained are therefore actual representations of the structure's vibration in its operational condition. The vibration obtained will be small, therefore sensitive and low-noise measurement equipment is necessary [17]. OMA is often used since it is fast and cheap, while EMA requires expensive and heavy devices. Also, performing an OMA will not affect the use of the structure.

2.4 Mathematical tools for application to MDOF systems

2.4.1 Autocorrelation

In operational modal analysis the system under evaluation is assumed to be linear, and the loading is assumed to have white noise characteristics [20]. This results in a random response vector, $y(t)$. The response is assumed to be ergodic with zero mean. The correlation function is defined as [14]:

$$R_{yy}(\tau) = E[y(t)y(t+\tau)]. \tag{2.9}$$

Since the signals are assumed ergodic, time averaging can be used. For the time average to be equal to the expected value, the signal must approach infinity:

$$R_{yy}(\tau) = \lim_{T\to\infty} \frac{1}{T} \int_0^T y(t)y(t+\tau)dt \tag{2.10}$$

A recorded system response is of finite length, thus, statistical errors are introduced, and the correlation function must be estimated instead:

$$\hat{R}_{yy}(\tau) = \frac{1}{T-\tau} \int_0^{T-\tau} y(t)y(t+\tau)dt, \qquad 0 \leq \tau < T \tag{2.11}$$

Statistical errors depending on the modal parameters, time length and lags of signal, are introduced when a finite time length is considered [20].

2.4.2 Spectral density

The Fourier transform of two sample records x(t) and y(t), of finite length T, of a stationary stochastic process is given by [17, p. 38]:

$$X(f,T) = \int_0^T x(t)e^{-i2\pi ft}dt \tag{2.12}$$

$$Y(f,T) = \int_0^T y(t)e^{-i2\pi ft}dt \tag{2.13}$$

The one-sided auto- and cross-spectral density functions for positive frequencies, are given by:

$$G_{xx}(f) = 2S_{yy}(f) = 2\lim_{T\to\infty}\frac{1}{T}E\Big[\big|X(f,T)\big|^2\Big] \tag{2.14}$$

$$G_{yy}(f) = 2S_{yy}(f) = 2\lim_{T\to\infty}\frac{1}{T}E\Big[\big|Y(f,T)\big|^2\Big] \tag{2.15}$$

$$G_{xy}(f) = 2S_{xy}(f) = 2\lim_{T\to\infty}\frac{1}{T}E\Big[X^*(f,T)Y(f,T)\Big] \tag{2.16}$$

The power spectral densities (PSDs) above can be obtained by *Welch' approach*. The procedure is based on the direct computation of the Fast Fourier Transform (FFT) of the sample records, and estimating the PSDs in agreement with equations (2.14)-(2.16). The procedure require operations on the sample signals in order to obtain good estimates.

According to equations (2.14)-(2.16), the one-sided spectral density function can be estimated by dividing the sample record into n_d continuous segments, each segment of length T=NΔt, and applying the Fourier transform on each segment. The auto-spectral density can then be computed through an ensemble averaging operation over the n_d data-subsets by the following [17, p. 42]:

$$\hat{G}_{xx}(f) = \frac{2}{n_d N\Delta t}\sum_{i=1}^{n_d}\big|X_i(f)\big|^2, \tag{2.17}$$

where N is the number of data points in each segment for determination of the FFT, and determines the frequency resolution of the estimates. The number of averages n_d determines the random error of the estimates.

As presented in [17], *leakage* can cause significant distortions when estimating the spectral density. Leakage arise when the record is divided into n_d segments, due to spreading of energy at a certain frequency to the neighbouring frequencies, causing large amplitude errors. This can be suppressed by making data periodic by tapering them by a certain time window, eliminating discontinuities at the beginning and end of the data records. In this thesis the *Hanning window* is used, which is the full cosine tapering window [17, p. 43] given by:

$$u_{Hanning}(t) = \begin{cases} 1-\cos^2\left(\frac{\pi t}{T}\right) & 0 \le t \le T \\ 0 & \text{elsewhere} \end{cases} \tag{2.18}$$

Despite minimizing leakage, the use of the Hanning window to compute spectral density estimates implies a loss factor of 3/8 [17, p. 43], causing a need to re-scale the spectral density estimates to obtain the correct magnitude. In addition to the loss factor, the half power bandwidth of the main lobe also increases when suppressing leakage, which may affect damping estimates [17]. The increase in half power bandwidth can be avoided if the segment length is increased, such that the FFT provides the same bandwidth with tapering as would have occurred without. An increase in tapered segment lengths implies an increase in total record length.

With a limited amount of data, increased tapered segment length is possible at the cost of the number of averages n_d. This cause the resulting PSD estimates variability to increase. Therefore, in the case of limited amount of data, n_d can be increased by dividing the total record length into partially overlapping segments [17, p. 43].

2.5 Frequency Domain Decomposition Method

The method is applied in order to estimate modal parameters, such as natural frequencies and modal shapes of recorded acceleration time histories.

The modal expansion of the structural response is given by

$$\{y(t)\} = [\Phi]\{p(t)\}, \tag{2.19}$$

where [Φ] is the modal matrix, and {p(t)} is the vector containing the modal coordinates. The auto-correlation matrix of the response becomes:

$$[R_{yy}(\tau)] = E\Big[\{y(t)\}\{y(t+\tau)\}^T\Big] = [\Phi]\big[R_{pp}(\tau)\big][\Phi]^T. \tag{2.20}$$

The first step is to estimate the PSD matrix:

$$G_{YY}(f) = \begin{bmatrix} G_{Y_1Y_1}(f) & G_{Y_1Y_2}(f) & \cdots & G_{Y_1Y_n}(f) \\ G_{Y_2Y_1}(f) & G_{Y_2Y_2}(f) & \cdots & G_{Y_2Y_n}(f) \\ \vdots & \vdots & \ddots & \vdots \\ G_{Y_nY_1}(f) & G_{Y_nY_2}(f) & \cdots & G_{Y_nY_n}(f) \end{bmatrix} \tag{2.21}$$

The diagonal elements (i = j, e.g. $G_{Y_1Y_1}$) denote the auto-spectral densities, while the off-diagonal elements ($i \neq j$, e.g. $g_{Y_1Y_2}$) denote the cross-spectral densities. By taking the Fourier transform of equation (2.20), the following relation is obtained:

$$[G_{YY}(f)] = [\Phi]\big[G_{PP}(f)\big][\Phi]^H, \tag{2.22}$$

where $G_{PP}(f)$ is the auto-spectral density matrix of the modal coordinates. If the modal coordinates are uncorrelated, the PSD of the modal coordinates is diagonal. The estimate of the output PSD, at discrete frequencies $f = f_i$, can be obtained by taking the Singular Value Decomposition (SVD) of the spectral matrix [17, p. 131], leading to the following factorization:

$$[G_{YY}(f)] = [U][\Sigma][U]^H, \tag{2.23}$$

where [U]=$[u_1, u_2, ..., u_m]$ is a unitary matrix containing the singular vectors, and $[\Sigma_i]$ is a diagonal matrix containing the scalar singular values arranged in descending order. The relationship between equation (2.22) and (2.23) shows that the singular values are related to the modal parameters [17, p. 131]. The singular values can therefore be used to establish the spectrum of corresponding SDOF systems characterized by the same modal parameters as the modes contributing to the

MDOF system evaluated. Due to the descending order of the singular values in $[\Sigma]$, at resonance, only the first singular value is sufficient to obtain information about of the dominating mode at the given frequency *f*. Close to a peak corresponding to the k-th mode in the spectrum, it is assumed that one mode will dominate. The PSD matrix will then only consist of one term, and can be written as:

$$[G_{YY}(f)] = \sigma_1 \{u_1\}\{u_1\}^H, f \to f_k \tag{2.24}$$

where σ_1 is the corresponding singular value belong to the auto PSD function of the equivalent SDOF system corresponding to the mode of interest [17, p. 130]. The first singular vector u_1 represents an estimate of the modal shape:

$$\{\hat{\phi}_k\} = \{u_1(f_k)\} \tag{2.25}$$

The SDOF PSD function is identified by isolating the peak and comparing the mode shape estimate with the singular vectors obtained for frequency lines around the peak [1, p. 168].

2.6 Analysis of Mode Shape Estimates

2.6.1 Modal Phase Collinearity

Modal analysis of the experimental results provide the modal estimates in the form of complex eigenvalues and eigenvectors [17, p. 179]. This leads to a distinction between normal modes, characterized by real-value mode shape vectors, and complex modes.

The post-processing of modal parameters is important because it provides measures of whether a complex mode shape estimate represents the dynamics of the structure, or if it is a result of other factors, such as gyroscopic effects, aerodynamic effects, non-linearities or non-proportional damping [9, p. 181]. One possible method to address the mode shape complexity is by calculating the Modal Phase Collinearity (MPC). It can be calculated by subtracting the mean of the r-th mode shape vector component:

$$\tilde{\phi}_{i,r} = \phi_{i,r} - \frac{\sum_{k=1}^{l} \phi_{k,r}}{l}, \quad i = 1, 2, ..., l \tag{2.26}$$

The MPC of the r-th mode shape is then given by

$$MPC_r = \frac{\left|\left| \operatorname{Re}\left(\{\tilde{\phi}_r\}\right)\right|\right|^2 + \left(\operatorname{Re}\left(\{\tilde{\phi}_r\}\right)^T \operatorname{Im}\left(\{\tilde{\phi}_r\}\right)\right)\left(2(\epsilon_{MPC}^2 + 1)\sin^2\theta_{MPC} - 1\right)/\epsilon_{MPC}}{\left|\left| \operatorname{Re}\left(\{\tilde{\phi}_r\}\right)\right|\right|^2 + \left|\left| \operatorname{Im}\left(\{\tilde{\phi}_r\}\right)\right|\right|^2}, \tag{2.27}$$

where

$$\epsilon_{MPC} = \frac{\left|\left| \operatorname{Im}\left(\{\tilde{\phi}_r\}\right)\right|\right|^2 - \left|\left| \operatorname{Im}\left(\{\tilde{\phi}_r\}\right)\right|\right|^2}{2\left(\operatorname{Re}\left(\{\tilde{\phi}_r\}\right)^T\right)\left(\operatorname{Im}\left(\{\tilde{\phi}_r\}\right)\right)} \tag{2.28}$$

$$\theta_{MPC} = \arctan\left(|\epsilon_{MPC}| + \text{sgn}\left(\epsilon_{MPC}\right)\sqrt{1+\epsilon_{MPC}^2}\right) \tag{2.29}$$

The MPC values are dimensionless and obtain a value between 0 and 1. Real modes will obtain an MPC value close to unity, while lower values indicate complex modes. A rejection level of 75 % has been chosen, hence modes with MPC<0.75 will not be accepted as real structural modes.

2.6.2 Modal Assurance Criterion

The Modal Assurance Criterion (MAC) is a useful tool for comparing two mode shapes. MAC is a measure used to quantify the correlation between two real-valued modal shape vectors, and is given by:

$$MAC\big(\{u_j\},\{\hat{\phi}_k\}\big) = \frac{\left|\{u_j\}^H\{\hat{\phi}_k\}\right|^2}{\big(\{u_j\}^H\{u_j\}\big)\big(\{\hat{\phi}_k\}^H\{\hat{\phi}_k\}\big)}, \tag{2.30}$$

where $\{\phi_k\}$ is the mode shape estimate at the peak of the k-th mode under investigation, and $\{u_j\}$ is the generic singular vector in the vicinity of the peak in the singular value plots. The MAC ranges between 0 and 1, representing inconsistent and perfectly consistent correspondence between the two mode shapes. A typically adopted MAC Rejection Level is about 0.8 [17, p. 132]. The MAC between analytical $\{\phi_A\}$ and experimental $\{\phi_E\}$ modal shapes are useful for verification and model updating [17, p. 187]. It is important to use recordings from several sensors in order to get good, reliable results from the MAC.

2.7 Structural Health Monitoring

Structural health monitoring (SHM) is the process of assessing the state of health of a structure, and predicting its remaining life [9, p. 3]. To strongly develop and implement the SHM process, sensor and material technology, modeling aspects and computing technology must be understood correctly. SHM has become a topic of interest for research of mechanical systems, offshore oil platforms, aerospace structures, aircrafts, civil infrastructures and buildings. These structures have in common that they all have finite life spans, and begin to deteriorate as soon as they are put into service [9, p. 3]. Damages in civil structures may be material or structural defects, formed during the stage of construction or during the structures service life, as a result from natural disasters or man-made actions [13]. Some examples of structural damage is corrosion, fatigue, erosion, wear and overloads. If these damages are not detected and repaired early, the maintenance cost would increase, as well as the structure would become unserviceable. In extreme cases, the structure would collapse causing fatalities and injuries. To prevent this, it is necessary to regularly carry out monitoring and detect structural damage at an early state. A number of actions can be taken depending on the value of the structure, the cost of repair and the consequences of failing [9, p. 3]. Ranged

by increasing sticker price relative to repair cost and criticality, the actions are: (1) wait until the structure breaks and dispose of it, (2) wait until the structure breaks and repair it, and finally (3) examine the structure at periodic intervals and determine whether remedial actions are needed or not. Many engineering structures, including bridges and buildings, fall under category 3. Bridge collapse is a possible consequence, therefore skilled engineers are needed to inspect structures regularly in order to asses the structural health.

The basic idea in SHM is providing the structure of interest with sensing and analysis capabilities, and to enable monitoring and evaluation to be carried out periodically or continuously, and autonomously [9, p. 4]. Potentially, SHM result in increased safety, avoids randomness of human behavior, and reduce ownership costs. The benefits of SHM are as follows [9, p. 4]:

- Allowing optimal use of structures, minimizing downtime, and avoidance of catastrophic failures;
- Giving the designer an improvement of his products; and
- Drastically change the work organization of maintenance services. This is achieved by introducing performance-based (or condition-based) maintenance (long term), or at least (short term) by reducing the present maintenance labor. In particular, dismounting of parts with no hidden defect can be avoided, and human involvement can be minimized. Thus, labor, downtime and errors can be reduced, and the structural safety and reliability improved.

A structural health monitoring system consists of hardware elements, such as sensors and associated instrumentation, and software elements, such as damage modelling and damage detection algorithms [9, p. 5]. Measurement data does not indicate defects or the type of defect in the structure. It is necessary to post-process the data in order to obtain meaningful quantities that benefit when locating defects, and quantify the severity of the defects. Therefore, modelling is an essential part of the SHM process. The Finite Element Method (FEM) is a common modelling tool, which is used to model damages in this thesis. It is important that the flaws can be detected by the FE model, thus, the mesh size must be fine in order to obtain accurate results of small flaws. This can result in large computational time, and FEM might not be a suitable method.

SHM has two essential components: the "diagnosis" and the "prognosis" [9, p. 5]. The diagnosis procedure determines the state of different parts in the structure, and the assembled structure as a whole. Hence, the outbreak of flaws and damages, their location and extent will be identified. The prognosis procedure determines the damage severity and the remaining life of the structure.

Generally, damage assessment can be defined at five levels [17, p. 309]. Ranged in increasing order of difficulty, the five levels are: (1) identification of damage existence, (2) localization of damage, (3) identification of the type of damage, (4) quantification of damage severity, and (5) ability to carry out a safety evaluation and prediction of the remaining service life of the structure. Researchers are still working on developing methods that are non-destructive, quantifiable and objective in order to achieve the five levels listed above.

Dynamics-based SHM techniques involves detecting and analyzing the dynamic response of a structure in order to evaluate the health of a component. These techniques are classified by [9, p. 14]: (1) the type of response being considered for the investigation, (2) the frequency range of interrogation, and (3) the modality used to excite the structural component. The SHM techniques can also be classified as "passive" or "active". If an external excitation source is not needed to evaluate the structural health of the system, the technique is classified as "passive". Hence, an "active" technique indicates the presence of damage by exiting an external source in order to generate a structural response. In this thesis, the structure under evaluation is a cantilever beam, thus mainly "active" techniques are used.

SHM techniques based on vibration usually includes the entire structural component, including the boundary conditions. Therefore, a detected damage can be a defect located anywhere within the structure. Vibration-based techniques are typically considered as "global" tools [9, p. 18]. During the design process of a component it is important to have knowledge about modal properties of the structure, and how they relate to the loading configuration. In most cases, variation of the modal properties indicates deterioration in structural performance, dictating maintenance, repair or replacement needs.

2.7.1 Damage-Sensitive Features

Different damage-sensitive features or parameters can be used in order to indicate the presence of damage in a structure. From the system response data, these quantities are extracted and used to accurately distinguish a damaged structure from an undamaged one [6, p. 161]. Through a process of feature extraction, the measured data is transformed to an alternative form, from which it is more readily to observe the correlation with the damage. The feature selection process determines which features to be used in a damage detection process. Features that are insensitive to operational and environmental variability, and only sensitive to the damage presence are most ideal. This is complicated in the real world as features that are sensitive to damage often are sensitive to changes in the system response not related to damage. When multiple types of damage occur, different types of features may be required in order to identify the different type of damages.

The damage sensitive parameters presented in this section assume that the measurements can be compared with results from the undamaged structure. In real life, this might be difficult since necessary information about the undamaged structure is not always available, and that the changes measured are only due to damage [9, p. 408].

Natural Frequency Shifts

Generally, when a structure is subjected to damage, the structural stiffness and/or damping ratio changes. In theory, changes in stiffness can be determined by natural frequency and mode shape variations. Natural frequencies provide the simplest way to detect the presence of damage [17, p. 309]. However, the natural frequencies only provide information sufficient to identify level (1) of damage detection. It should

be pointed out that natural frequency shifts do not necessarily provide adequate information to uniquely identify the damage by itself [6, 9, 17]. Frequency shifts are relatively insensitive to damage, thus, very accurate measurements or severe damages are required for this feature to identify damage.

Mode Shapes

When detecting small damages, mode shapes and their spatial derivatives are more effective, and better at locating the damage. Mode shapes provide spatially distributed information about the dynamic characteristics of the structure, and therefore offer the ability to locate the damage as well as establish the existence of damage [6, p. 197]. This feature needs a large number of sensors to achieve the required spatial resolution in order to characterize the mode shapes, and therefore estimated with less accuracy compared to natural frequencies.

Mode Shape Curvature

The Mode Shape Curvature (MSC) method is an alternative method to mode shapes, based on the mode shape derivatives. Beams have a direct relationship between curvature and bending strain. At a given location, x, the curvature, $v''(x)$, is approximated by [6, p. 207]:

$$v''(x) \approx \frac{M(x)}{EI}, \tag{2.31}$$

where E is the Young's modulus, and I is the moment of inertia of the beam cross-section. From this equation, it is evident that for a given moment, $M(x)$, applied to the structure, a reduction of stiffness related to damage leads to an increased curvature. This structural effect can be used to detect and localize damages. The mode shape curvature of a beam can be estimated using central difference approximation as [6]:

$$v''(\phi_i) \approx \frac{\phi_{i-1} - 2\phi_i + \phi_{i+1}}{h^2}, \tag{2.32}$$

where h is the distance between equally spaced measurement points along the beam length. The curvature at the beam ends can be approximated by backward and forward difference operators. Equation (2.32) gives the curvature for a given mode shape, ϕ_i, at the measured coordinate, i. The MSC for multiple modes can be used as a damage indicator for a particular location [6], and is given by

$$MSC = \left| \left(\phi^D\right)'' - \left(\phi^U\right)'' \right|, \tag{2.33}$$

where $\left(\phi^D\right)''$ and $\left(\phi^U\right)''$ indicates damaged and undamaged mode shape curvatures.

If cracks, or other damages, are introduced in a structure, it reduces the stiffness of the structure, at the cracked section or in the damaged region, increasing the curvature magnitude in the section. The curvature changes are local in nature, hence, it can be used to detect and locate cracks and damages. The change in

curvature increase as the stiffness reduce, therefore the amount of damage can be obtained from the magnitude of change in curvature [16].

When sensors are placed with unequal spacing the finite difference scheme suggested in equation (2.32) no longer applies. Therefore, a finite difference approximation for a non-linear node spacing has been derived. A non-uniform 3-point mesh can be considered [18]:

$$M_x = \{a < b < c\}, \tag{2.34}$$

where the variable steps are denoted as $h_1 = b - a$ and $h_2 = c - b$. By assuming that $h_1, h_2 > 0$, and the function $f(x)$ is a sufficiently smooth function attaining the values $\{f(a), f(b), f(c)\}$, the second derivative approximations can be developed by expanding the Taylor series of $f(a)$ and $f(c)$ about the $x = b$:

$$f(a) = f(b) - h_1 f'(b) + \frac{h_1^2}{2} f''(b) + ... \tag{2.35}$$

$$f(c) = f(b) + h_2 f'(b) + \frac{h_2^2}{2} f''(b) + ... \tag{2.36}$$

By solving equation (2.35) and (2.36), the following is obtained:

$$f''(b) = \frac{2}{h_1(h_1 + h_2)} f(a) - \frac{2}{h_1 h_2} f(b) + \frac{2}{h_2(h_1 + h_2)} f(c) \tag{2.37}$$

The central difference approximation with unequally spaced sensors can then be rewritten as:

$$f''(b) = \alpha f(a) + \beta f(b) + \gamma f(c), \tag{2.38}$$

where the coefficients α, β and γ are regarded as the weights, defined as:

$$\begin{aligned} \alpha &= \frac{2}{h_1(h_1 + h_2)} \\ \gamma &= \frac{2}{h_2(h_1 + h_2)} \\ \beta &= -\alpha - \gamma \end{aligned} \tag{2.39}$$

The order of accuracy of the derivative approximations are higher for the uniform mesh, due to the lack of symmetry of the non-uniform meshes. The accuracy improves for ratios between h_1 and h_2 close to unity.

The beam is mounted with bolts at $x = 0$ giving the boundary condition

$$f(x = 0) = 0 \tag{2.40}$$

The boundary node makes equation (2.38) valid for the very first sensor closest to the boundary. The following is given by Euler-Bernoulli beam theory

$$M = -EI \frac{d^2 f(x)}{dx^2}. \tag{2.41}$$

As there are no moments at the end of a cantilever beam, the second boundary condition is $f''(L) = 0$.

Modal Flexibility

The flexibility matrix $[G]$ is defined as the inverse of the stiffness matrix $[k]$ [6]:

$$\{f\} = [k]\{y\} \Rightarrow \{y\} = [k]^{-1}\{f\} = [G]\{f\}, \tag{2.42}$$

where $\{f\}$ is the vector of applied static loads, and $\{y\}$ is the deformation vector associated with the static loads. Equation (2.42) shows that a reduction in the stiffness matrix will cause an increase in the flexibility matrix. The indices of the flexibility matrix G_{ij} are defined as the displacement at DOF i caused by an applied unit load in DOF j. Hence, the columns of G are deformation patterns the structure will assume when a unit load is applied at the DOF associated with the column.

If an undamaged structure has m mass-normalized modal shapes, obtained from experimental data for n degrees of freedom, the $n \times n$ flexibility matrix can be approximated as [6]:

$$[G] = [\Phi][\Lambda]^{-1}[\Phi]^T \approx \sum_{i=1}^{m} \frac{1}{\omega_i^2}\{\phi\}_i\{\phi\}_i^T, \tag{2.43}$$

where $[\Phi]$=$[\phi_1, \phi_2, ..., \phi_m]$ is the mode shape matrix, $[\Lambda]$=diag(ω_i^2) is the modal stiffness matrix, $\{\phi\}_i$ and ω_i are the i-th mass-normalized modal shape and modal frequency. The scaling factor $1/\omega_i^2$ reduces the influence of the higher order modes when estimating the flexibility matrix. The flexibility change caused by damage can be obtained from the difference between the flexibility matrices of the undamaged $[\mathrm{G}]_U$ and damaged $[\mathrm{G}]_D$ structure:

$$[\Delta G] = [G]_U - [G]_D \tag{2.44}$$

The maximum absolute value of all elements in the j-th column of ΔG is defined as:

$$\overline{\delta}_j = \max_j |g_{ij}|, \quad i = 1, 2, ..., n \tag{2.45}$$

where g_{ij} are elements of $[\Delta G]$, measuring the flexibility change at each degree of freedom i. The column j corresponding to the largest $\overline{\delta}_j$ indicates the damaged degree of freedom.

Since the Modal Flexibility method requires mass-normalised mode shapes, challenges can arise when using data obtained from experimental vibration tests. The method can still be used to locate damage if the mode shape normalization is consistent [6].

Statistical Moments

Sensors along the structure y_i record time series of finite length n. Different statistics can be used to identify changes in the structural response due to damage. Some of these statistical moments are listed in table 2.1. In the case of damage, the stiffness of the system will be reduced, thus, the peak amplitude in (2.46) of the

measured response will typically increase. Mean values, such as the mean in (2.47) and the root-mean-square in (2.48), can be used to measure the typical value of a probability distribution, as well as the data span. It should be noted that the mean value is sensitive to outliners, meaning a few data points can significantly influence the feature [6, p. 174]. In such cases, the median can be used instead as it is less sensitive to outliners. The variance in (2.49) measures the amount of variation

Table 2.1: Signal statistics used as damage-sensitive features obtained from [6].

Peak amplitude (y_{peak})	$y_{peak} = \max \lvert y_i \rvert$	(2.46)
Mean ($\overline{y}$)	$\overline{y} = \frac{1}{n} \sum_{i=1}^{n} y_i$	(2.47)
Root-mean-square (RMS)	$RMS = \sqrt{\frac{1}{n} \sum_{i=1}^{n} (y_i)^2}$	(2.48)
Variance (σ^2)	$\sigma^2 = \frac{1}{n} \sum_{i=1}^{n} (y_i - \overline{y})^2$	(2.49)
Skewness (dimensionless) (γ)	$\gamma = \frac{\frac{1}{n} \sum_{i=1}^{n} (y_i)^3}{\sigma^3}$	(2.50)
Kurtosis (dimensionless) (κ)	$\kappa = \frac{\frac{1}{n} \sum_{i=1}^{n} (y_i)^4}{\sigma^4}$	(2.51)

with respect to the mean of the time-series amplitudes. A stiffness reduction due to damage will generally tend to increase the variance of measured response, such as acceleration [6, p. 175]. Another useful statistical moment is the skewness in (2.50), which measures the symmetry of the probability distribution of a random variable about its mean. Therefore, symmetrical distributions such as the Gaussian distribution, will have a skewness of zero. The kurtosis in equation (2.51) is a measure of the peaked nature of the distribution of the measured response. A Gaussian distributed response will have a kurtosis equal to 3 [6, p. 177].

2.8 Statistical Principles

In the early stage of damage detection it is important to take the uncertainty of damage related parameters into account, in order to distinguish small, physical changes from statistical variability [5]. Parameters estimated from vibration measurements can have statistical uncertainties, hence, it is important to distinguish statistical uncertainties from actual damage. In this section, statistical properties important for evaluation of measurement data for damage identification in SHM are presented.

2.8.1 The Gaussian Distribution

The Gaussian (or normal) distribution is one of the most important probability density functions (PDFs), as it is completely fixed by knowledge of its mean and variance [6, p. 131]. In statistics there is a big field of study to identify what kind of distribution a series have. In many cases the income data are either right or left skewed. This thesis will not perform this study, but assume that the data are Gaussian distributed. The Gaussian PDF is

$$p(x) = \frac{1}{\sqrt{2\pi\sigma^2}} exp\Big\{ -\frac{1}{2}\Big(\frac{x-\overline{x}}{\sigma}\Big)^2 \Big\} \tag{2.52}$$

The shape of the Gaussian PDF is bell shaped, and often referred to the as the bell curve.

2.8.2 Confidence interval

The confidence interval is a type of estimate computed from the observed data. The main purpose of the confidence interval is to indicate the precision of the sample study [2]. The width of the confidence interval is associated with standard deviation, sample size and the degree of confidence. The most usual degree of confidence is 95%. The 95% confidence level means that there is a 95% probability that the interval covers the data parameter [10].

2.8.3 Bhattacharyya distance

The Bhattacharyya distance measures the similarity of two probability distributions, in terms of mean value and standard deviation. For two normal distributed series, p and q, the Bhattacharyya distance, B, is calculated as [4]:

$$B(p,q) = \frac{1}{4} ln\left(\frac{1}{4}\left(\frac{\sigma_p^2}{\sigma_q^2} + \frac{\sigma_q^2}{\sigma_p^2} + 2\right)\right) + \frac{1}{4}\left(\frac{(\mu_p - \mu_q)^2}{\sigma_p^2 + \sigma_q^2}\right), \quad 0 \leq B \leq \infty \tag{2.53}$$

where σ_p and σ_q are the standard deviations of the two series, and μ_p and μ_p the means. Two identical distributions will have $B = 0$, while unequal distributions will have large B values.

Chapter 3

Case Study

A case study of a cantilever beam was performed to investigate different methods and features for damage identification. The main part of the study was based on acceleration measurements done in the laboratory. A numerical model was also established in order to find an optimal sensor layout, as well as testing the damage impact before the real-life cantilever was subjected to damage. The first section presents dimensions and material properties of the cantilever beam, before the FE model and the experimental setup is presented An experimental and numerical system identification are presented and compared, before the implementation of the different damage scenarios are introduced.

3.1 The Cantilever Beam

The cross-section of the cantilever beam is shaped as a +, with a height and width is 152mm, and a thickness of 2.5mm. The support consists of a welded end-plate with a height of 100mm, a width of 320mm, and a thickness of 10mm. A systematic overview of the beam and plate dimensions are shown in figure 3.1. The welded end-plate was mounted to a rigid wall by four bolts with a diameter of 22mm. In between the wall and the end-plate, four steel rings were placed in order to obtain pinned connections. The aluminum beam was assumed to have a Young's modulus of 68.9GPa, a Poisson's ratio of 0.33, and a density of 2700kg/m^3. Since the exact material properties were not known or established from testing, the numerical results may differ slightly from experimental results.

3.2 The Numerical Model

A Finite Element model of the cantilever was created to evaluate the beam before conducting experiments in the laboratory. The FE model was evaluated so that the optimal sensor layout could be decided. The cantilever beam and end-plate were created as a shell model in ABAQUS using 8-noded shell elements (S8R).

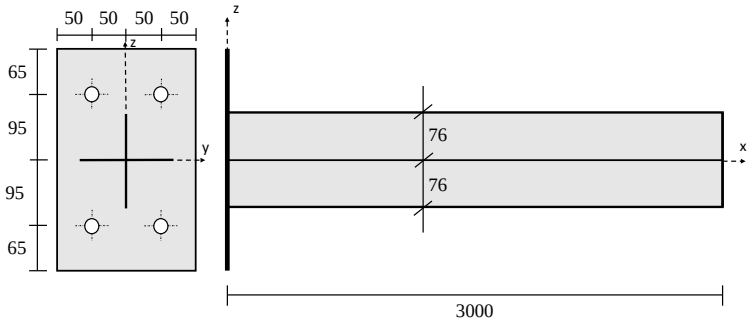

Figure 3.1: Cantilever beam and end-plate dimensions [mm].

The mesh size of the beam was set to 10x10mm, as shown in figure 3.2. The bolt holes in the end-plate were meshed using partitioning.

The aluminum beam is subjected to lateral and vertical bending, as well as torsion. Due to the cross section of the beam, the modes of vibration are mainly dominated by torsion. Figure 3.3 shows the first two torsional, vertical and lateral modes of the cantilever. In the frequency range 0-320 Hz, the modal analysis of the cantilever beam resulted in 24 modes. The eigenvalue analysis of the beam resulted in the natural frequencies listed in table 3.4.

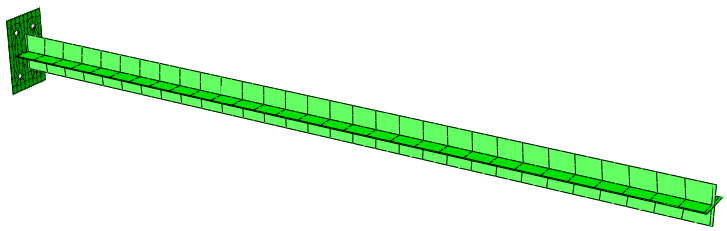

Figure 3.2: Finite element model of the cantilever beam.

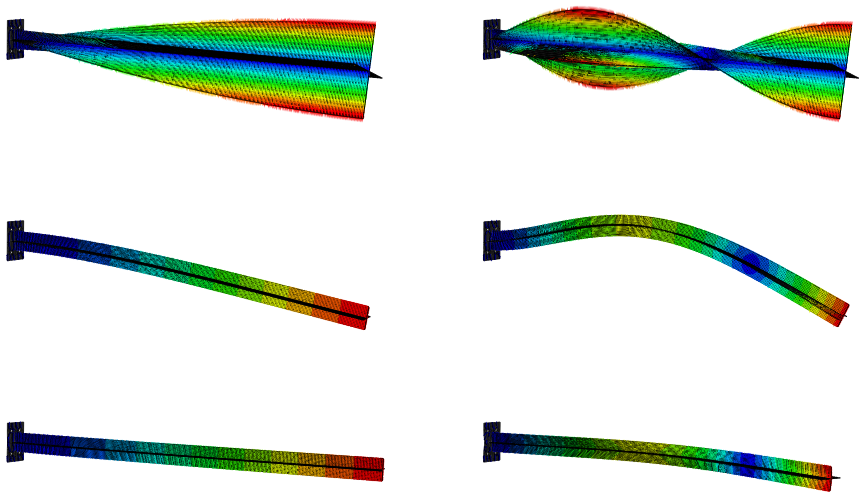

Figure 3.3: First and second torsional mode (top), vertical bending mode (middle) and lateral bending mode (bottom).

3.2.1 Introducing Rayleigh Damping

The Rayleigh Damping coefficients of the cantilever beam were estimated by the approach described in section 2.2. The significant mass participation factors and natural frequencies were obtained from the eigenvalue analysis. Figure 3.4 shows the three different calculation approaches, as well as the linear regression estimation. The three approaches resulted in the estimates listed in table 3.1. The first

Table 3.1: Rayleigh damping coefficient estimates.

Approach	α	β
Linear regression	1.5693	$1.6818e^{-05}$
72nd mode approximation	1.6474	$4.0138e^{-05}$
Full range approximation	1.6474	$3.0211e^{-05}$
Average data approximation	1.6474	$3.5175e^{-05}$

approach evaluated the first 72 modes. An initial damping ratio of ζ_1=2% for the first mode, and a damping ratio of $\zeta_{m=72}$=5% for the 72^{nd} mode was chosen. For the second approach, a total of M=2.5 $\cdot$ m=179 modes were included in the calculation of the Rayleigh damping coefficients. The approach was based on ζ_1 and $\zeta_{M=179}$=11%, obtained from the first approach. The third approach was calculated from the average values of the first and second approach. Table 3.1 shows no varia-

tion in the α-values of the three different approaches, and small β-values. The final coefficients are chosen based on the results in figure 3.4, which clearly shows that the method including the entire range of modes, i.e all 179 modes, correlates best with the linear regression. Therefore, the Rayleigh Damping coefficient estimates used in the FE model were $\alpha_2 = 1.6474$ and $\beta_2 = 3.0211e^{-05}$.

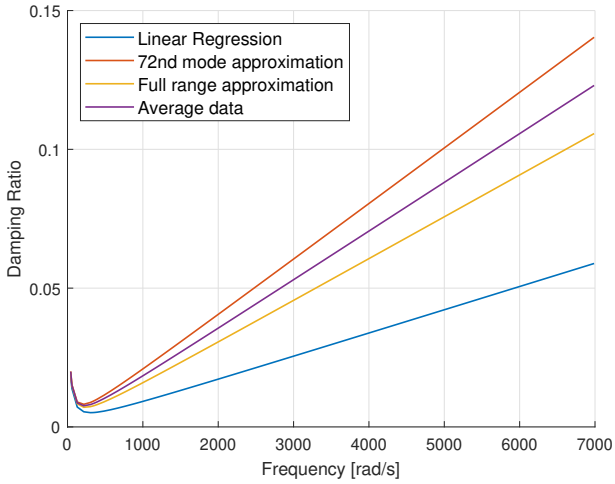

Figure 3.4: Estimations of damping ratios

3.3 Placing of Sensors

The purpose of finding the most optimal sensor layout is to be able to measure the response of all modes in the experimental tests. Optimal sensor placement is an essential topic in SHM and there exists numerous automatic methods to determine the optimal sensor layout numerically. However, due to time constraints and the scope of this thesis, a manual approach with trial and error was used. A sensor layout was chosen based on an overall assessment of the modes from the eigenvalue analysis of the cantilever beam, and the ability to identify these modes with FDD.

3.3.1 Modal Analysis of Numerical Model

The dynamic characteristics of the aluminum cantilever beam were estimated by the FDD method. Firstly, a static analysis was performed, using Simpsons integration rule with 5 thickness integration points and a shell thickness of 1mm. An initial force of 20N was placed on the right edge of the cantilever shown in figure 3.2. The prescribed force was released, and the dynamic behavior of the beam was evaluated. The time increment, dt, in the dynamic analysis affect the accuracy of the natural frequency and mode shapes estimates. A time increment of 0.0016

seconds was chosen. The natural frequencies obtained form the modal analysis are listed in table 3.4.

3.3.2 Sensor Layout

In order to use as few accelerometers as possible, to identify as many modes as possible, sensors were placed at every L/3 and L/4 resulting in a total of 7 sensors. Figure 3.5 shows the sensors rotating around the x-axis as they are placed over the length. The coordinates of the sensor locations are listed in table 3.2. The

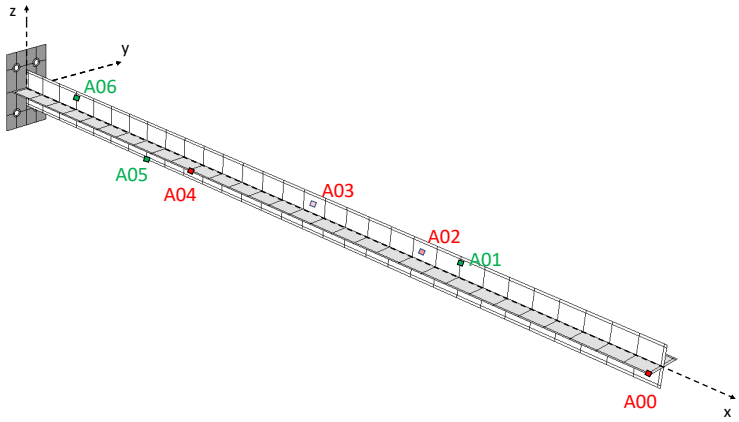

Figure 3.5: Sensor layout.

strength of the sensor layout was established by evaluating the mode shapes of the eigenvalue analysis with the mode shapes estimated by FDD. The first 24 modes estimated by FDD correlate well with the first 24 modes of the eigenvalue analysis, as figure 3.6 shows. The off-diagonal terms increased when fewer sensors were used, but it was still possible to uniquely identify modes up to 24. Mode 3, 15 and 20 obtained low MAC values, while modes 21, and 24 to 28 were not possible

Table 3.2: Coordinate position of sensors.

Sensor	**Coordinates [mm]**		
	x	**y**	**z**
A00	2990	-66	0
A01	2200	0	66
A02	2000	66	0
A03	1500	66	0
A04	1000	-66	0
A05	700	0	-66
A06	300	0	66

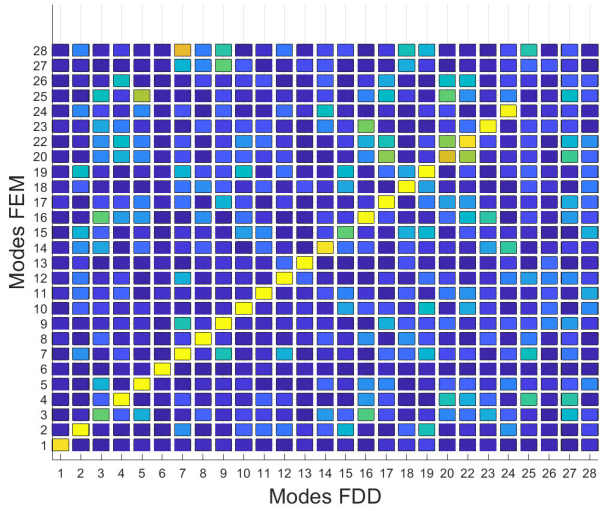

Figure 3.6: MAC matrix of FEM and FDD (7 sensors) mode shapes.

to estimate with the chosen sensor layout. These modes might therefore be hard to identify during the experiments in the laboratory. The results obtained in this section justify the sensor layout in figure 3.5, and this was therefore used in the experimental damage identification analysis.

3.4 Experimental Setup

As a consequence of the national shut-down, due to Covid-19, the experimental study was postponed. In the laboratory, a total of 7 triaxial piezoelectric accelerometers were used for the output-only modal analysis. The accelerometers used were *Dytran series 3583BT* with a maximum sampling frequency of f_s=640Hz, making them capable of measuring frequencies up to 320Hz. The beam was examined under ideal environments as the experiments were carried out in the laboratory. The yellow wall in figure 3.7 was mounted in the middle of the room, thus not a

Table 3.3: Execution of all the laboratory tests.

Time [min]	**Action**
0-1	White noise
1	Vertical tap flange
2	Vertical tap web
3	Horizontal tap web
4-5	White noise

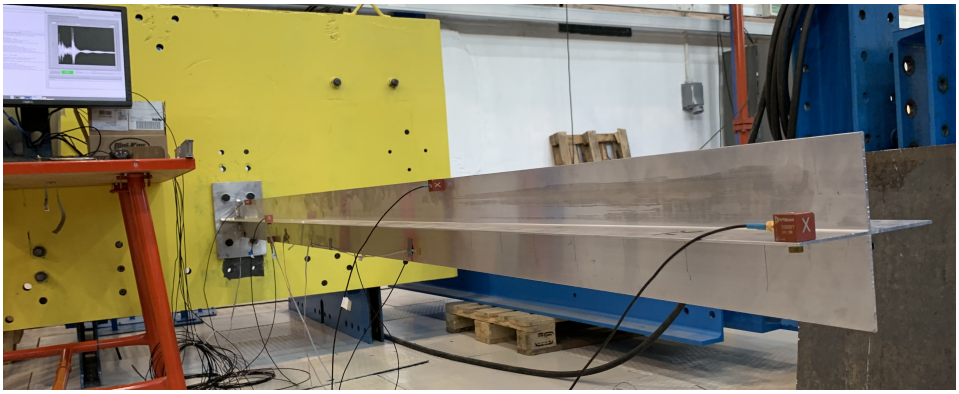

Figure 3.7: Laboratory setup.

part of the load carrying system of the building. However, the wall was mounted to the floor, which may cause other experiments or people walking by to affect the results.

Before introducing damages to the beam, the system identification of the experimental data was performed, and compared to the eigenvalue analysis of the FE model. In this way the strength of the laboratory setup, the FE model, and the system identification can be evaluated. As seen in figure 3.9(a), the cables were taped to the beam. This was done to avoid unnecessary noise from the measurement equipment, and eliminate a possible source of error.

The tests have been executed by the loads described in table 3.3. The first and last minutes of the recording consists of white noise response. After each loading, the beam was left to vibrate for one minute, before a load was applied in a different direction. Different loadings were applied in order to execute all torsional, vertical and lateral modes.

3.4.1 System Identification of the Undamaged Beam

The dynamic characteristics of the cantilever beam were estimated by output-only modal analysis (OMA), and the Frequency Domain Decomposition (FDD) method was applied to evaluate the measurement data. Figure 3.8 shows the first singular value frequencies up to 220 Hz obtained for one of the acceleration recordings. In Norway, a three-phase alternating current with $f \approx$50Hz is used in the public distribution network. Therefore, the SV peak observed around 48Hz is not a peak caused by dynamic vibration. The system identification resulted in a total of 24 modes listed in table 3.4. The SV peaks were easy to identify for the first 18 modes, therefore only these modes have been evaluated in the damage identification in chapter 4.

Table 3.4: Experimental (FDD) and numerical (FEM) frequencies of the cantilever beam.

	Experimental		**Numerical**	
Mode no.	**Frequency [Hz]**	**Type**	**Frequency [Hz]**	**Type**
1	7.90	Bending (Lateral)	8.31	Bending (Lateral)
2	8.82	Torsion	8.50	Torsion
3	9.04	Bending (vertical/torsion)	9.35	Bending (Vertical)
4	26.46	Torsion	25.72	Torsion
5	43.80	Torsion	43.00	Torsion
6	50.87	Bending (Lateral)	53.33	Bending (Lateral)
7	55.80	Bending (Vertical)	57.95	Bending (Vertical)
8	61.61	Torsion	60.47	Torsion
9	80.26	Torsion	78.20	Torsion
10	97.55	Torsion	96.27	Torsion
11	115.98	Torsion	114.76	Torsion
12	133.37	Torsion	133.72	Torsion
13	141.52	Bending (Lateral)	147.03	Bending (Lateral)
14	149.55	Bending (Vertical)	153.25	Torsion
15	156.33	Torsion	155.25	Bending (Vertical)
16	177.29	Torsion	173.39	Torsion
17	194.85	Torsion	194.23	Torsion
18	211.48	Torsion	215.84	Torsion
19	242.20	Torsion	238.27	Torsion
20	246.42	-	261.62	Torsion
21	255.78	-	261.75	Bending (Lateral)
22	268.17	-	270.75	Bending (Vertical)
23	272.13	-	286.96	Torsion
24	286.44	-	311.36	Torsion

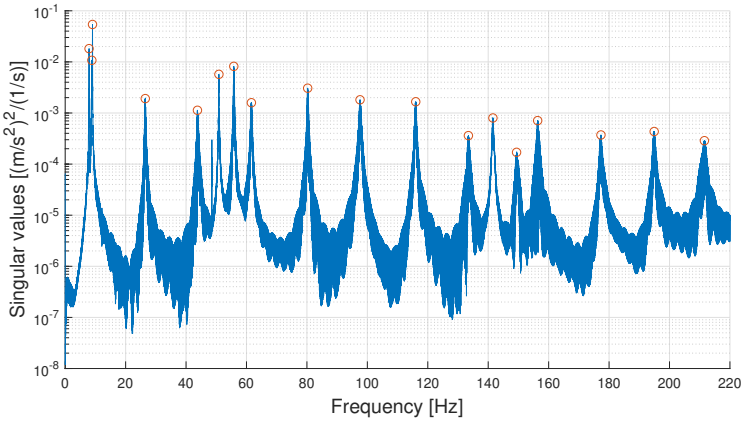

Figure 3.8: 1st singular value.

3.4.2 Damage Scenarios

Three different damage scenarios were evaluated in the numerical and experimental damage identification studies. The three scenarios are point mass, cuts and removal of bolts, and the experimental and numerical implementations are presented below.

Experimental Implementation of Damages

There was only one test piece available for the thesis, so it was crucial to apply damages in the correct order. In order to limit the damage extent of the beam, point masses (M) were added to the beam instead of reducing the stiffness. The point masses were added in (2990, 66, 0) referring to coordinate system in figure 3.5. The four weights used for testing are listed in table 3.5. Before any permanent damages were done to the beam, tests were performed with loose bolts. The three boundary damages (B) are listed in table 3.5. The coordinates in the table indicates

Table 3.5: Summary of experimental damage cases.

M [kg]	**B [mm]**	**C [mm]**	**CR [mm]**
0.05	(0, -50, 95)	1	40
0.1	(0, -50,+/-95)	10	70
0.25	(0,+/-50, -95)	20	
1.0		40	
		60	
		70	

which bolt that was removed. The first boundary damage (B1) was removal of one top bolt, the second (B2) was the removal of two side bolts, and the last (B3) was the removal of two bottom bolts. The last damage case applied were cut damages. First cuts (C) were only applied to the web in (1000, 0, 76), but due to low values of the evaluated features, another cut was added in the flange at (1000, 76, 0), resulting in CR-damages. The different cut depths evaluated in the laboratory are listed in table 3.5. A total of 15 damages have been evaluated, where each damage was subjected to vibrations 10 times, so that outliers and poorly executed experiments would be detected. A summary of the experiments carried out can be found in table A2-A5 in Appendix A. Figure 3.9 shows the experimental setup of the different damage types.

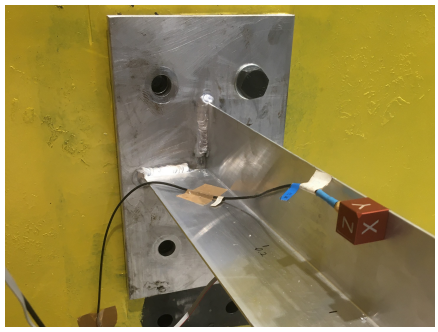

(a) B2-damage

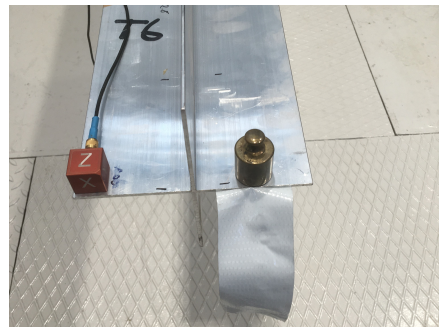

(b) M-damage

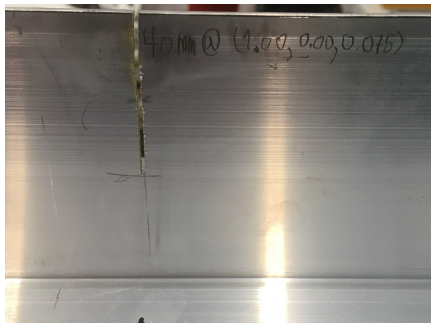

(c) C-damage

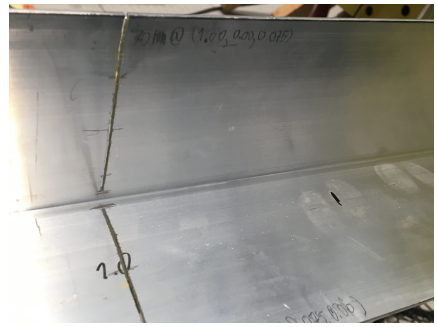

(d) CR-damage

Figure 3.9: Experimental set up of damages.

Numerical Implementation of Damages

In finite element analyses, damages can be implemented in several ways. In ABAQUS the point mass was implemented as an Engineering Feature. The point mass should be a part of the structure and not an external load. In this way the point mass can be included in the modal analysis. The point mass was therefore included as

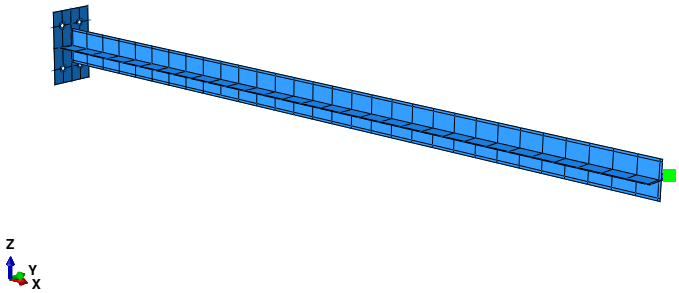

Figure 3.10: Implementation of point mass

inertia with isotropic mass. No damping was added to the point mass. Figure 3.10 illustrates the point mass as a green square on the edge of the beam. The cuts were created using partitioning. Since the FE model of the beam was made of S8R elements, the partitioning was done by making a partitioning face in the sketch. Figure 3.11 shows the implemented 40 mm cut in the web, with a thickness of 1mm. By partitioning, the material in the area remains unchanged, which was the case in the experiments. For a mesh size of 10x10mm, the cut hardly influences the mesh. ABAQUS did not report any warnings at the triangular elements.

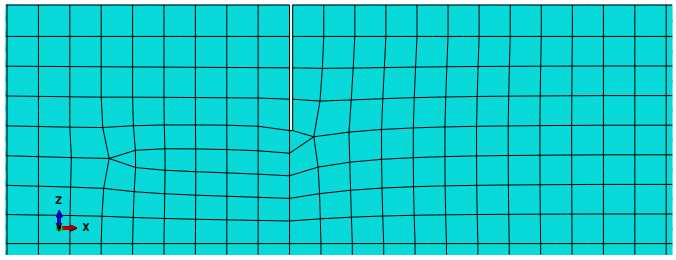

Figure 3.11: Implementation of a 40 mm deep cut.

In the laboratory the beam was attached to the wall by four bolts where spacers were placed between the end-plate and the wall. These bolts were implemented as boundary conditions in ABAQUS. The area of the spacers was implemented as circle partitions around the holes of the bolts. The boundary conditions were assigned to the circles as Encastre, meaning U1=U2=U3=UR1=UR2=UR3=0. The boundary condition was Encastre because the plate was rigid in the area where the bolt and the spacer were mounted. Figure 3.12 shows the implementation of the removal of two side bolts.

The different damage scenarios were analysed in two ways: Modal Analysis

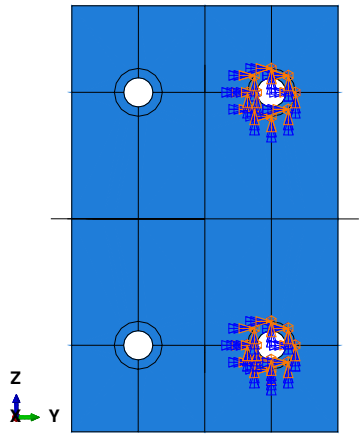

Figure 3.12: Implementation of removed bolts.

and FDD of the time series. The time series contains two white noise loads at the edge of the beam, one lateral and one vertical. The white noises created in Matlab were included in ABAQUS as load amplitudes. Two loads in two different directions were applied, such that all modes would be excited. In this way the system identification will be more similar to actual white noise.

Chapter 4

Results and Discussion

The goal of the study was to determine which damages that could be identified by means of acceleration measurements, how large the damage must be before it could be identified, and whether the severity of identified damages could be determined from the measurement data. In this chapter, natural frequency shifts, mode shapes, curvature and modal flexibility are investigated as features for experimental modal analysis parameters. Also, statistical moments of the recorded response histories are evaluated. The numerical study is included to support experimental finds and exclude possible errors.

4.1 Natural Frequency Shifts

The experimental study of frequency shifts was based on the mean frequencies of each damage. Figure 4.1 shows the natural frequencies and the relative frequency error of the point mass damages. The figure shows that the largest point masses (M3 and M4) result in the largest frequency shifts. The heavy point mass errors drops considerably for mode 3. At first sight it seems incorrect as the mode was the first vertical mode. The mode shape analysis shows that the mode was not established, and it is therefore not good for comparison. The frequency shifts are not as visible for the lower point masses (M1 and M2) as the error is approximately 1%.

Figure 4.2 shows the natural frequency shifts when the cantilever was subjected to boundary damages. The boundary damages follow a similar frequency pattern for all three damages. The first lateral bending mode 1 obtained a high relative error of nearly 40% when removing two side bolts (B2). The bolt removal caused a lateral stiffness reduction, i.e. a large reduction of the natural frequencies of the lateral bending modes. The frequency error dropped with approximately 35% for mode 2. The removal of two bottom bolts (B3) caused a relatively high frequency shift of nearly 30% for the first and second mode. The two damage types differ, in that the B2 damage caused the largest frequency shifts mainly for lateral bending modes, while the B3 damage for both lateral and vertical bending modes. The

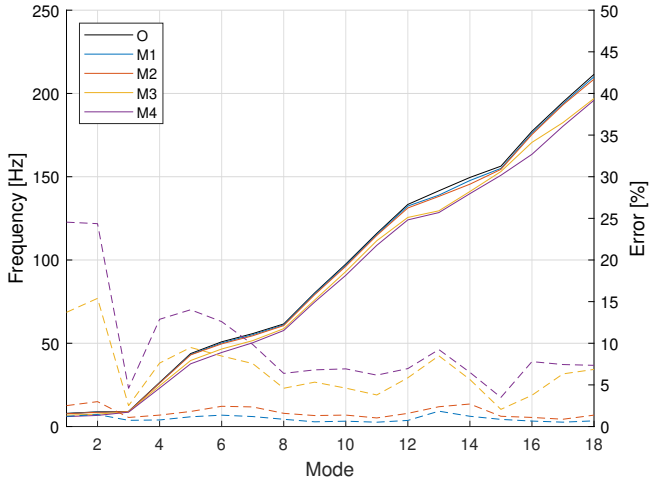

Figure 4.1: Natural frequency and relative error of M-damages.

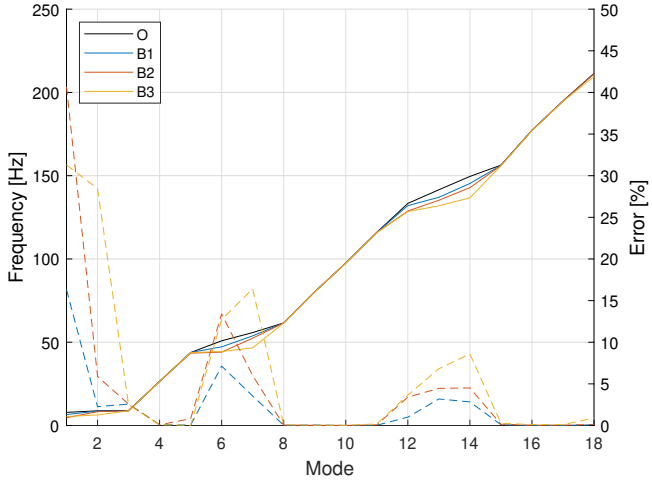

Figure 4.2: Natural frequency and relative error of B-damages.

removal of one top bolt (B1) resulted in a frequency shift of around 15% for the first mode. The B1 damage caused similar frequency shifts as the B2, though slightly lower. The torsional behavior of the cantilever beam was hardly affected by any of the boundary damages, as the natural frequencies of the torsional modes did not shift. With this observation the B-, and M-damages are distinguished. The frequencies of the M-damage shifted at every mode, while the frequencies of the B-damages only shifted in the bending modes.

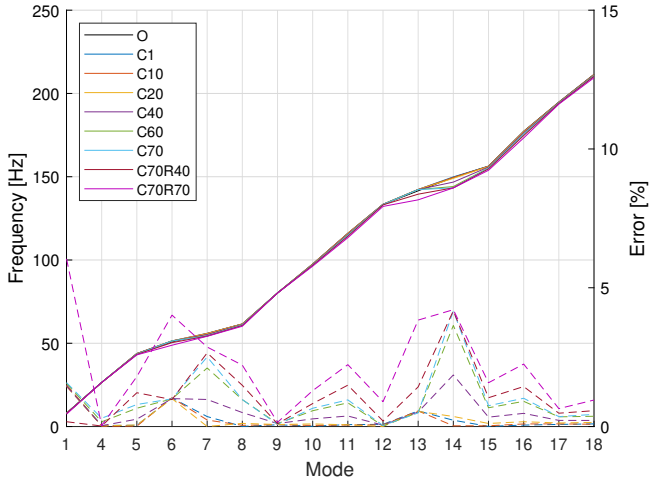

Figure 4.3: Natural frequency and absolute relative error of C- and CR-damages.

The frequency shifts of the cut damages are shown in figure 4.3. The lower cut damages C1 to C40 resulted in small frequency shifts, making them hard to identify. The FDD method estimated 17 modes instead of 18 of C60, C70, C70R40 and C70R70, indicating a merging of the second and third mode. This will be investigated in the following section about mode shapes. Since only natural frequencies were analyzed, both mode 2 and 3 were excluded, such that the frequency pattern of the C- and CR-damages can be illustrated properly. Figure 4.3 shows that cuts in both web and flange increased the frequency compared to cuts in the top web only. The C-damages obtained peaks for mode 1, 6, 7, 11, 14 and 16. When the CR-damages were introduced the relative errors of mode 6 and 13 increased significantly. Modes 4, 9 and 12 hardly shifted for the cut damages. The frequency error in figure 4.3 clearly increased with increasing cut depth.

The natural frequency shifts were used to evaluate the strength of natural frequencies as damage indicators. Feature vectors were established for each damage case before the MAC matrix was calculated. The natural frequency shift feature vector for each damage was established as:

$$\vec{d} = [\Delta f_1 \quad \Delta f_4 \quad \Delta f_5 \quad ... \quad \Delta f_m], \tag{4.1}$$

where

$$\Delta f_i = \overline{f}_{i,U} - \overline{f}_{i,D}, \qquad i = 1, 4, ..., m \tag{4.2}$$

where m is the number of modes, U indicates the undamaged beam and D indicates the damage scenarios listed in table 3.5. The higher cut damages only recorded 17 modes, hence mode 2 and 3 were also excluded from the natural frequency feature vector comparison. The MAC matrix of the frequency shift feature vectors is shown in figure 4.4. The damage classes show different frequency patterns. An

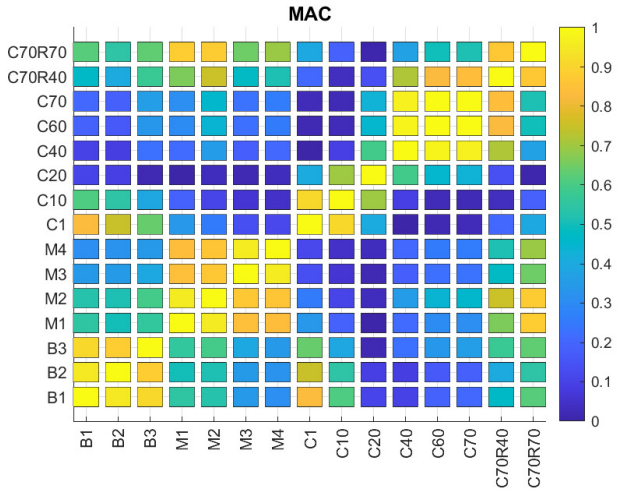

Figure 4.4: MAC matrix of frequency shift feature vectors.

interesting observation is that the lower levels of the C-damage did not correlate with the higher levels. Due to small frequency shifts, it was necessary to evaluate whether a damage was an actual damage or just a deviation from the estimated natural frequencies of the undamaged beam. Figure 4.5 shows the 5th and 95th percentiles of the first 8 natural frequencies of the damaged beam compared to the confidence interval of the undamaged beam. If the estimated damaged frequency is within the frequency domain of the undamaged beam, the damage will be classified as undamaged. The figure shows that the damaged frequencies deviates from the undamaged beam for some modes. The undamaged frequency domains of modes 1 to 18 are presented in table A6 in Appendix A.

Figure 4.5 clearly illustrates how the natural frequency decreased as the point mass increased, which corresponds with the relationship $\omega_n = \sqrt{k/m}$. For B-damages the frequencies vary more depending on which bolts that were removed, and what kind of mode that was analyzed. For the first and second lateral mode (1 and 6), the removal of two side bolts resulted in the lowest fundamental frequency, hence the largest shift. For the first and second vertical modes (3 and 7), the removal of two bottom bolts obtained the lowest frequency and largest shift. For such severe damages some of the modes shifts. It is re-emphasized that this will be analyzed in the following section 4.2.

It is obvious that the cuts provide the smallest frequency shifts. For the C-damages, where the cut was made in the cross-sectional web, the vertical stiffness decreased. By investigating the vertical modes (3 and 7), the frequency drop was detected for a 40mm deep cut. For the CR-damages, the lateral stiffness did decrease. These were severe cuts and did therefore affect the lateral and torsional modes. From the lateral modes (1 and 6), the frequency drop was detected for a 40mm cut.

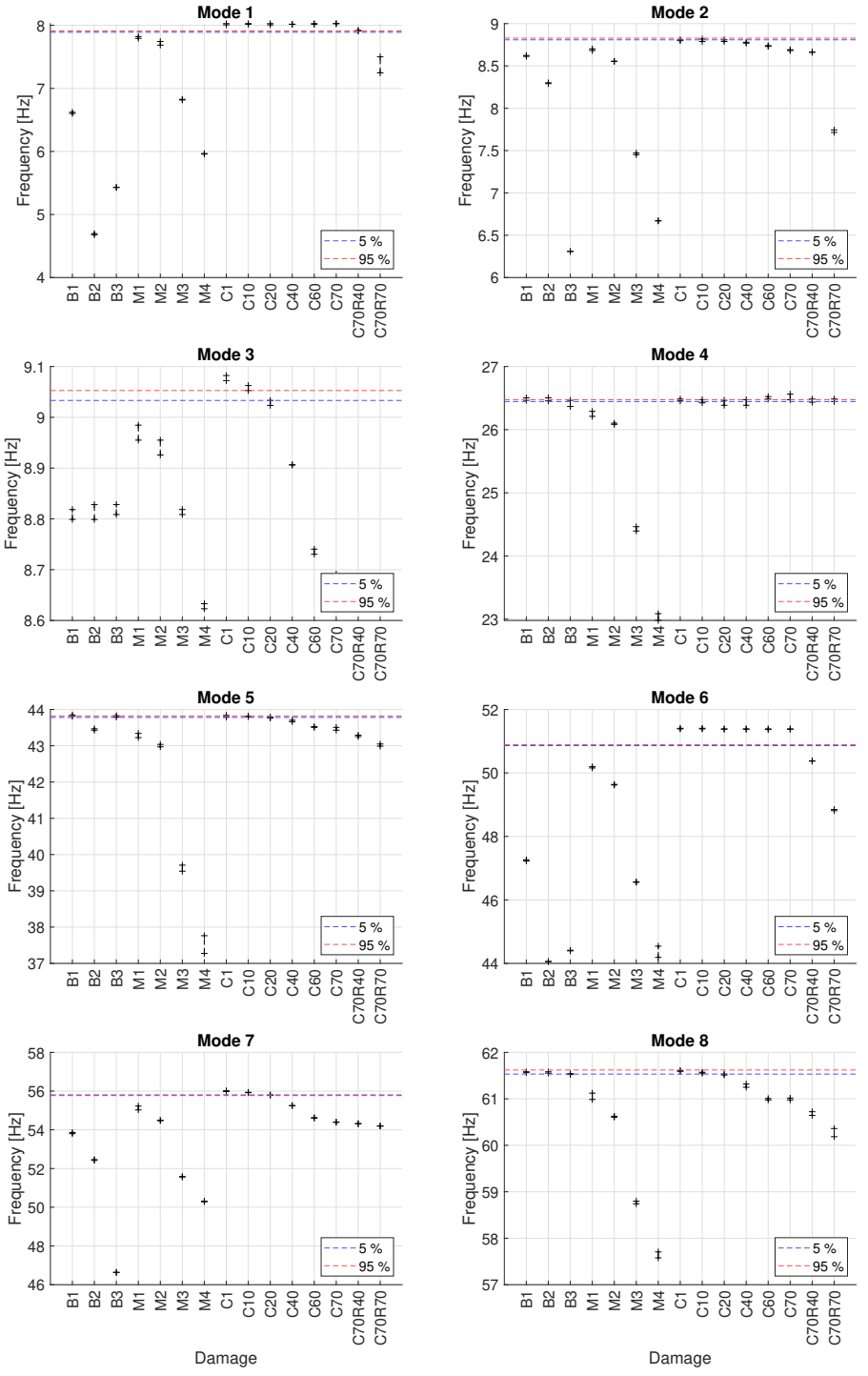

Figure 4.5: Confidence interval of undamaged beam and percentiles of damages.

For the smallest cuts the frequency of mode 1, 3 and 6 did increase, which was not expected. From the numerical study the frequencies deviated at the vertical modes only. Section 4.2 obtains high MAC values for these mode shapes, which indicates that the correct mode has been examined. The increase of frequencies was not obtained for any other damage scenario, but it occurred for several cuts. Therefore, it is hard to tell if there was an error in either the original tests or the cuts. A possible explanation to the increased frequency, is that the B-damages have been introduced in-between the measurements of the undamaged beam and the C-damages. When the B-damages were reversed, the cantilever beam could have been mounted in a slightly different way, as the mounting was done by different people. In that way, the stiffness of the boundary could have been changed, resulting in a frequency increase.

In order to evaluate other statistics, the probability distributions were established from the 10 tests. The natural frequencies are assumed to be Gaussian distributed based on the mean and standard deviation of the system identifications. A way to distinguish the probability distribution of the undamaged beam with damaged ones is to calculate the Bhattacharyya distance. The Bhattacharyya distance of the four damage types are plotted in figure 4.6(a)-(d).

The confidence intervals in figure 4.5 clearly showed frequency shifts for the M- and B-damages. These observations were approved by the Bhattacharyya distances where the M- and B-damages in figure 4.6(a)-(b) obtained high values for the bending modes. In figure 4.6(c) a cut depth of 40mm was detected in the vertical modes (3, 7 and 14). The CR-damages in figure 4.6(d) show that the Bhattacharyya distances also increased for the lateral modes.

When measuring natural frequency shift, it is necessary to have many measurements in order to make sufficient estimates of the statistical variations. A large number of measurements will give better estimations of the probabilities for separating damages and deviations. The recorded natural frequencies were assumed to be Gaussian distributed, which may be incorrect. The distributions are often approximated from a bar plot, but a bar plot from 10 tests does not make a good approximation. The 5th and 95th percentile for the undamaged beam are listed in table A6 in Appendix A. According to [6, 11] errors of type I and type II can occur, meaning that a system can be withdrawn from service even though it is healthy, or a damaged system can continue operating in a damaged state. The acceptance/significance level is set to 5%, in order to prevent type II errors that could potentially threaten the structural safety, or result in a complete loss of the structure and human life.

In both the numerical and experimental study, the natural frequency decreased as the point mass increased. The relative error of the frequency shift of M1 and M2 is between 0-3% as shown in figure 4.1, while M3 and M4 obtained much higher errors in the domain-between 3-25%. Figure 4.5 clearly shows that even the smallest point mass of 0.05kg was detected by frequency shifts. In future studies, it would have been interesting to evaluate the point mass damage level that is required in order to record a mass damage by natural frequency shifts. The removal of bolts caused the lateral and vertical bending modes to shift significantly in natural

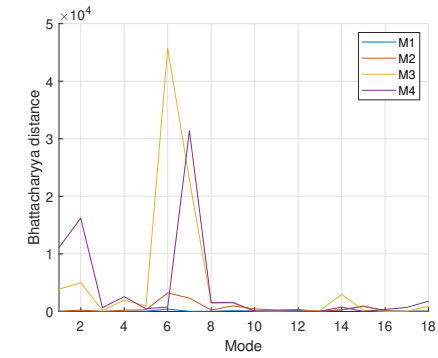

(a) M-damages.

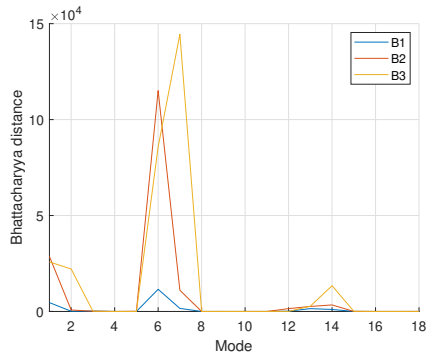

(b) B-damages.

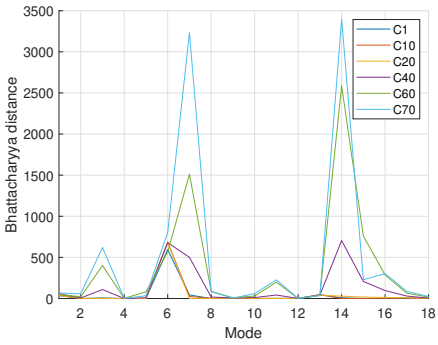

(c) C-damages.

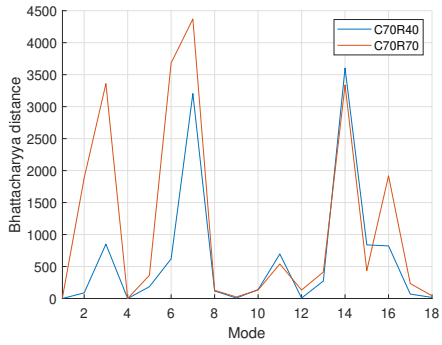

(d) CR-damages.

Figure 4.6: Bhattacharyya distance of M, B and C damages.

frequency. The errors in figure 4.2 indicate that the first modes have errors between 15-40%, depending on which bolts that are removed. When removing bolts the modes are rearranged, which will cause errors at the wrong modes. Even if the figure gives errors at some torsional modes, the error peaks are in the area where the bending modes originally were. When studying figure 4.5 the B-damages were not detected in most torsional modes, but deviated at the bending modes. This differs from the point mass damage where the frequency dropped at every mode.

The natural frequency shift feature vector manages to identify the presence of damage in the structure. Based on the results presented in this section, it is also possible to classify the different damages into M, B and C damages. By observing which modes that were shifting, B2- and B3-damages could be differentiated as well.

4.2 Mode Shapes

Mode shapes contain more information about the structural behavior than natural frequencies, as they give a representation of the actual deformation. In order to determine whether there was a damage present or not, a MAC acceptance level was determined. The MAC confidence interval of the undamaged cantilever was established by comparing the mode shape estimates of the 10 tests. Damaged modes with MAC values lower than the acceptance level were classified as damaged. Since the arguments are probabilistic, errors in the diagnosis can be a problem. The

Table 4.1: Percentiles of MAC values of undamaged beam.

Mode	**5%**	**2%**	**Mode**	**5%**	**2%**
1	0.9977	0.9975	10	0.9997	0.9997
2	0.8724	0.8375	11	0.9997	0.9997
3	0.9598	0.9553	12	0.9983	0.9979
4	0.9995	0.9995	13	0.9967	0.9959
5	0.9996	0.9993	14	0.9946	0.9944
6	0.9987	0.9986	15	0.9967	0.9955
7	0.9991	0.9987	16	0.9979	0.9977
8	0.9993	0.9990	17	0.9983	0.9975
9	0.9998	0.9998	18	0.9945	0.9944

2nd and 5th MAC percentiles of the undamaged beam are listed in table 4.1. If damages occur in-between the 2nd and 5th percentile, they should be investigated further.

By establishing the average mode shape matrix $\overline{\Phi}$, possible deviations can be excluded. The average mode shape matrix was calculated by:

$$\left[\overline{\Phi}_D\right] = \frac{1}{N}\sum_{i=1}^{N}\left[\Phi_{D,i}\right], \tag{4.3}$$

where D indicates the damage scenarios in table 3.5, and N are the 10 test performed of each damage. Figure 4.7 to 4.10 show the MAC matrices of the average damaged and undamaged mode shapes. The correlation between the M-damaged and the undamaged beam are shown in figure 4.7. The magnitude of the point mass strongly affected the dynamic behavior of the cantilever. As the point mass at the cantilever tip increased, the MAC values became more distorted. The M1 damage showed a slight reduction of MAC values of mode 2 and 3, which decreased as the point mass increased. The second point mass damage level also obtained a merging of mode 12 and 13. As the mass increased for M3 and M4, several mode shapes merged and switched. Figure 4.7 indicates that the point mass must be of a certain level before it starts changing the dynamic behavior of the system.

Figure 4.8 shows the MAC matrices of the three different boundary damages. All the B-damages affected the first three mode shapes. Both B1 and B2 reduced the vertical stiffness in such a way that the vertical mode became the second mode.

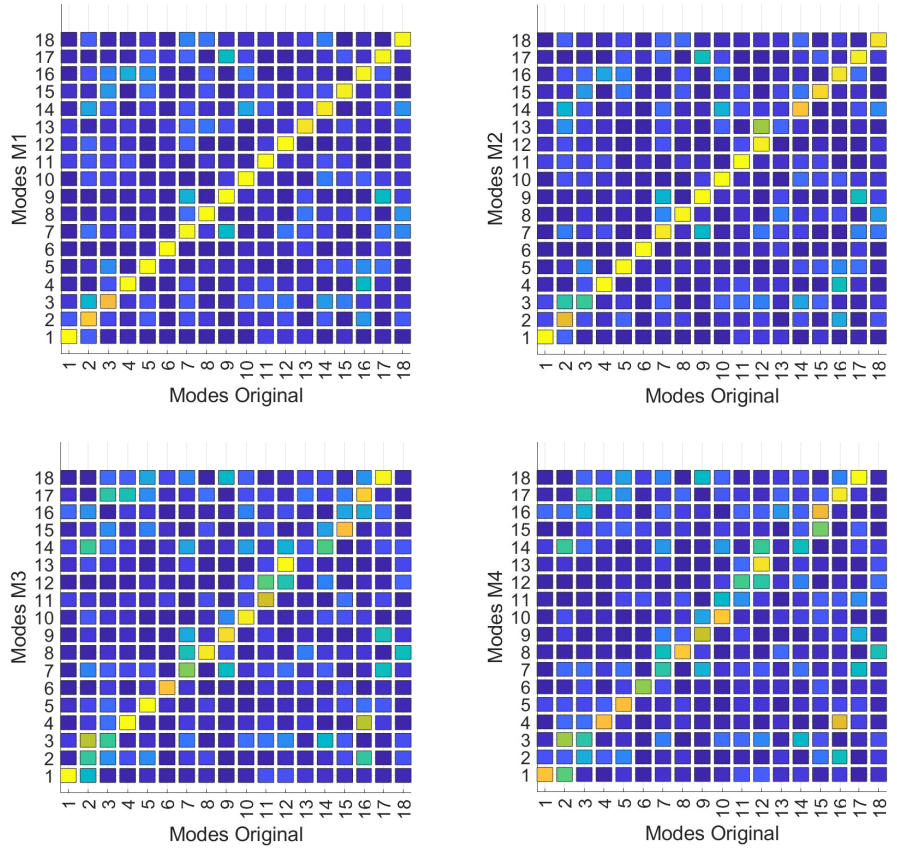

Figure 4.7: MAC matrices of M-damages.

The B3 damage reduced the vertical stiffness further, as the first vertical mode became the first fundamental mode. Removing two top or side bolts obtained a larger effect on the system than removing one. The MAC matrices of the point mass damages indicate that the M-damages changed the mode shapes, while the B-damages caused shift of the mode shapes.

The MAC values for the cut damages and the undamaged beam are shown in figure 4.9 and 4.10. The figure shows that cuts had to be at least 60mm deep to obtain any changes in the dynamic behavior. The original mode 2 of the undamaged beam could not be identified, and the MAC value of mode 3 have been reduced. This also applied to C70R40 in figure 4.10. The increased cut depth from 40 to 70 mm reduced the MAC of mode 13 heavily.

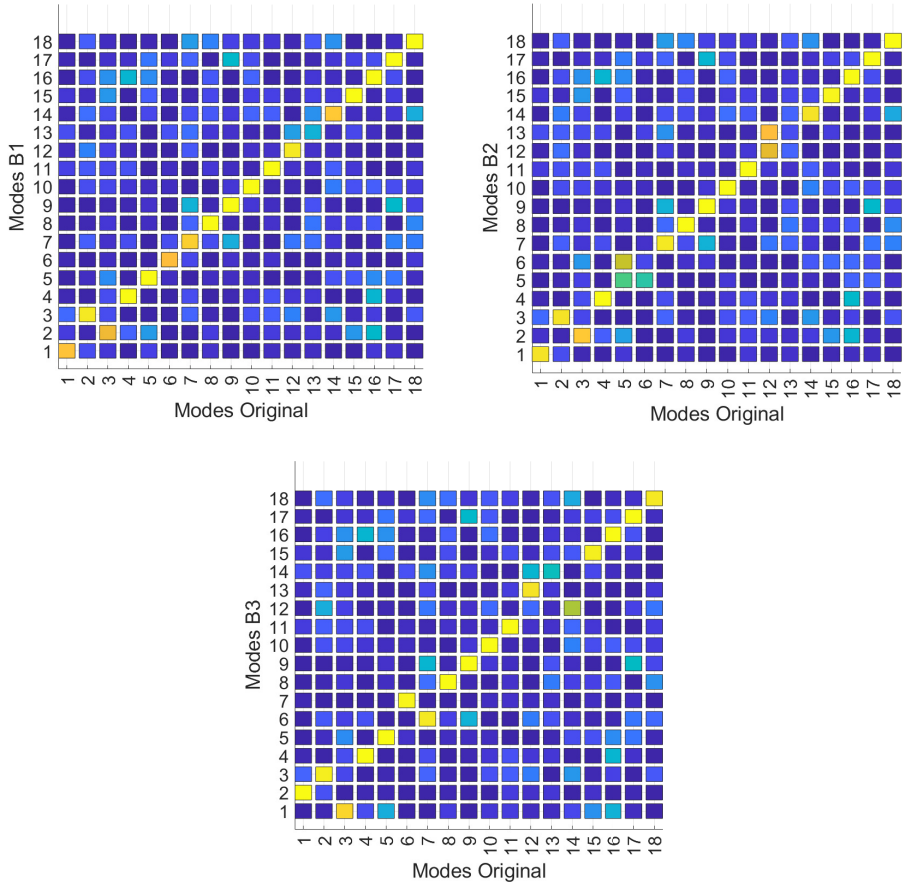

Figure 4.8: MAC matrices of B-damages.

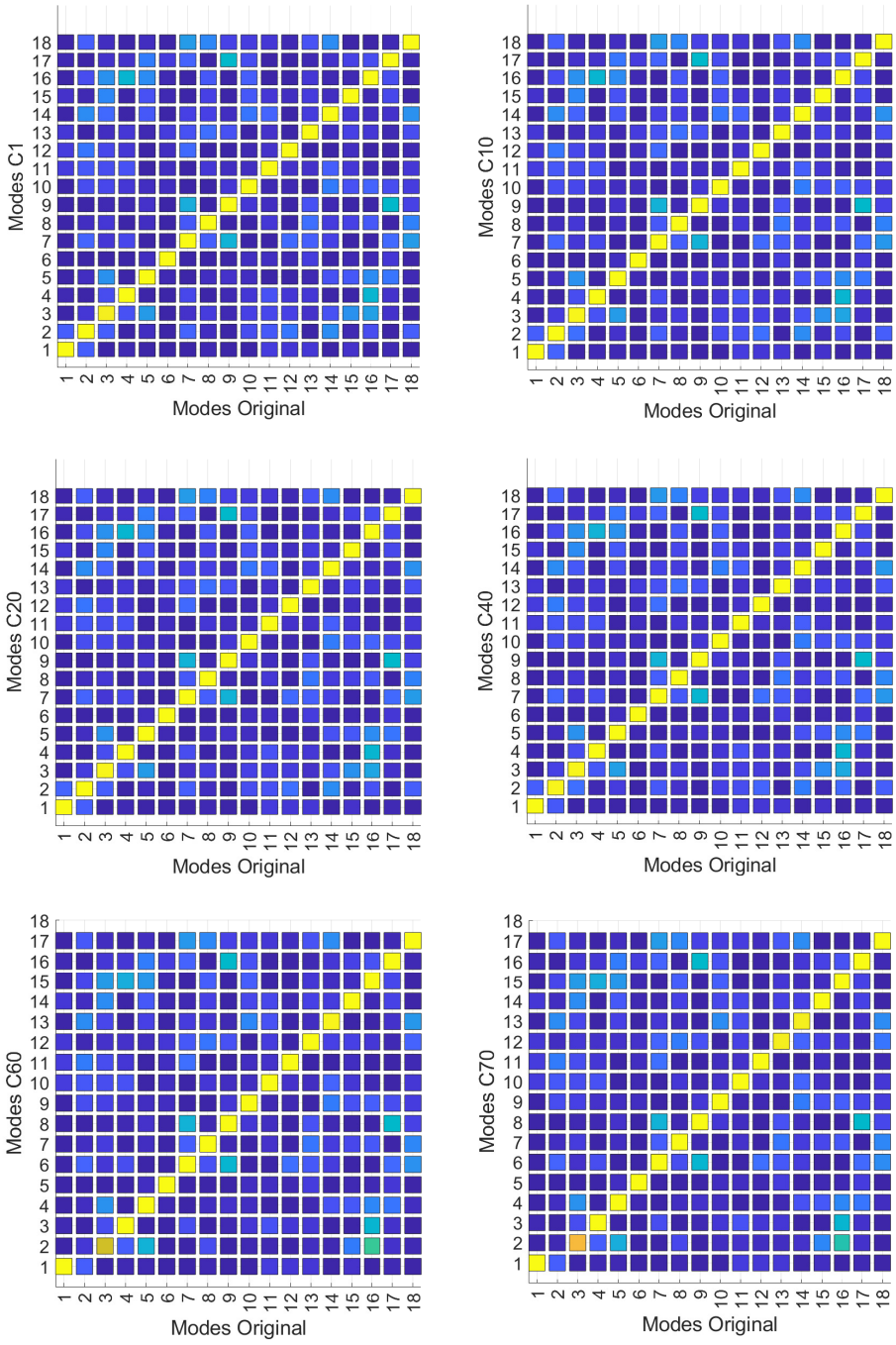

Figure 4.9: MAC matrices of C-damages.

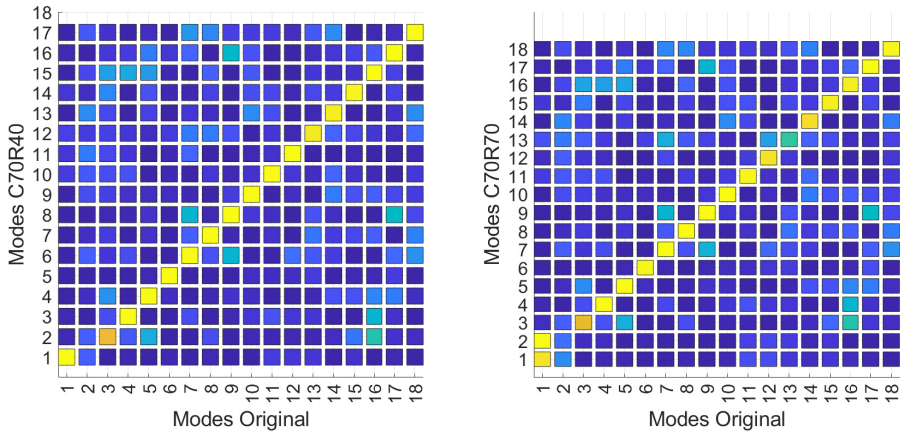

Figure 4.10: MAC matrices of CR-damages.

Mode shape feature vectors were established for each damage so that the different damages could be compared. The feature vectors were established by rearranging the average mode shape matrix in equation (4.3), to feature vector:

$$\vec{d} = \begin{bmatrix} \overline{\phi}_{*,1} & \overline{\phi}_{*,2} & \overline{\phi}_{*,3} & \dots & \overline{\phi}_{*,18} \end{bmatrix}. \tag{4.4}$$

The correlation between the resulting mode shape feature vectors were evaluated by the modal assurance criterion. Figure 4.11 shows the resulting MAC matrix of the M-, B-, C- and CR-damages, as well as the undamaged (O) mode shape feature vector. The figure shows high correlation between the C-damages, however five of the C-damages correlate well with the lower point mass damages (M1 and M2) and the undamaged beam. High correlation with the undamaged mode shapes indicates no damage present in the structure. The MAC matrix indicates that modal shapes, as a damage sensitive feature, are sensitive to the size of the damage. It is worth pointing out that M1 and M2 show high correlation with other mode shapes, while the higher point masses only obtain high correlation with the other point mass damages. This raises an interesting question about the necessary damage size needed for using mode shapes as damage indicator. Based on the results of the MAC matrix, the necessary point mass should be somewhere between 0.1kg and 0.5kg. Figure 4.11 also shows that B-damages can be distinguished from all other recorded mode shapes.

The mode shapes of the numerical model were not influenced by close modes, and all modes were classified as either pure bending or torsion. The modes of the experimental cantilever were influenced by local and closely spaced modes. Especially, the first vertical bending mode (mode 3) which was influenced by torsion in real life.

By combining the MAC matrix in figure 4.11 with the MAC matrices in figure 4.7-4.8 all of the M-, and B-damages can be identified. The M1-damage did not affect the structure much, but a damage was detected when comparing it with the

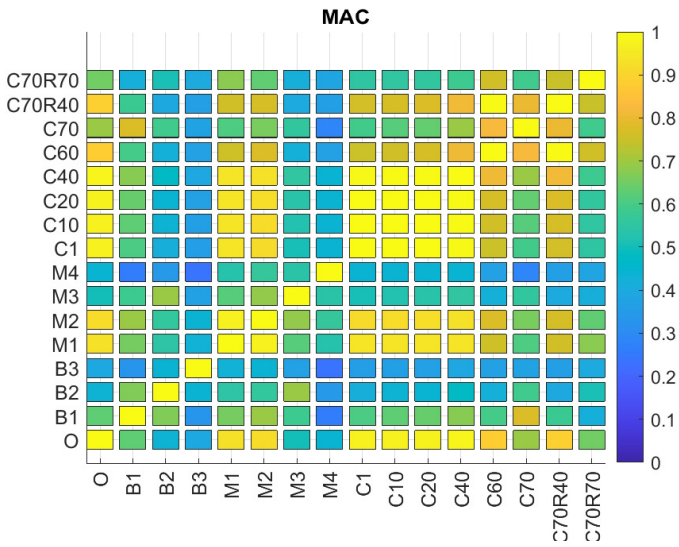

Figure 4.11: MAC matrix of damages based on average mode shapes.

values in table 4.1. An interesting observation about the boundary damages was the rearranged mode order due to the decrease of natural frequency of the pure bending modes. The rearranging was significant to the boundary damage compared to the point masses.

By studying figure 4.9, the cuts must be significant in order to be identified as a damage in the structure. For the 60mm cut, mode 2 and 3 merged, and mode 2 could not be identified. Also, mode 3 obtained a lower MAC value. This observation was also made for the CR-damages. For the 40mm flange cut, there were no obvious changes in the MAC matrix compared to the C70 damages. When increasing the flange cut to 70mm, mode 13 could not be identified. In further work, it would be interesting to investigate if it is possible to estimate the cut depth based on the decrease in MAC values. Also, if a critical level for the cut depth can be estimated in order to estimate the damage level necessary to obtain changes in the mode shape feature.

The mode shape feature reached damage assessment level (3), identification and classification of damage. Still, the method did not locate damages.

4.3 Mode Shape Curvature

Mode shape derivatives, such as curvature, can be used as an alternative to the mode shape feature for structures that exhibit bending behavior. The derivative will amplify discontinuities in mode shapes, which have been subjected to damage. Figure 4.12 and 4.13 show the mode shape curvature of different C and CR damages in x=1.0m. All of the mode shapes have been analyzed, but it was the first lateral

and vertical mode that gave the best results considering locating the damage. The grey lines illustrate the MSC of all 10 damage recordings, and the black line shows the mean MSC. The figures show large curvature peaks in x=2.0m for both modes, which clearly is a misinterpretation of the damage location. As the cut depth

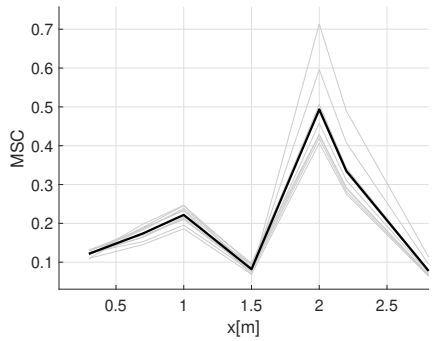

(a) First lateral mode of C40.

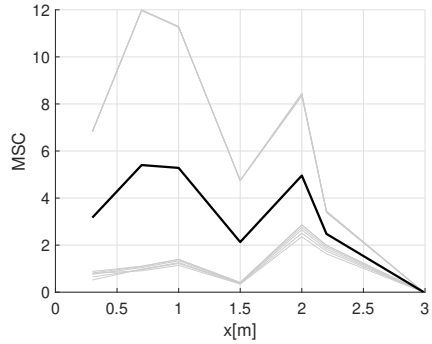

(b) First vertical mode of C40.

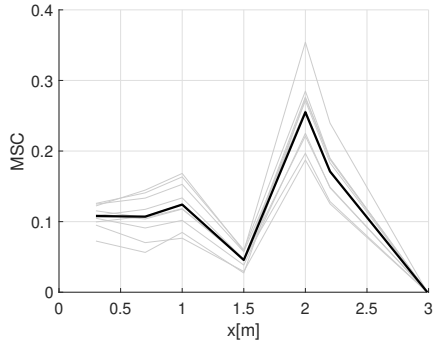

(c) First lateral mode of C60.

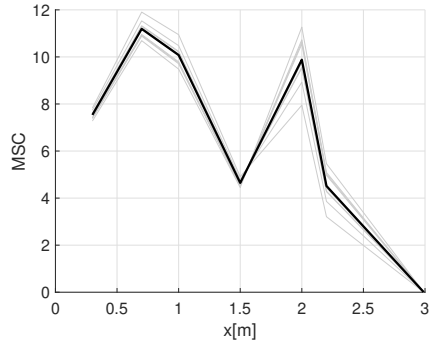

(d) First vertical mode of C60.

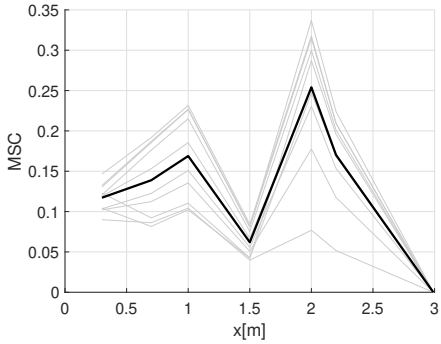

(e) First lateral mode of C70.

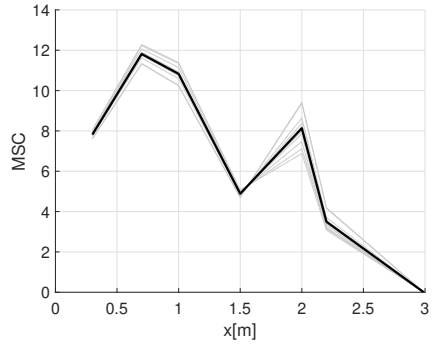

(f) First vertical mode of C70.

Figure 4.12: Experimental MSC of C-damages.

increase, the magnitude of the lateral MSC decrease, as figure 4.12(a), (c) and (d) illustrates. The vertical mode in figure 4.12(b), (d) and (f) shows that the peak in x=2.0m decrease relative to the peak in x={0.7, 1.0}, as the cut depth increases. However, the curvature obtains the largest peak in x=0.7m and the damage is still localized incorrectly.

The first lateral mode of the CR-damages in figure 4.13(a) and (c), obtains the larges MSC in two points along the x-axis. The lateral mode of the C70R70 damage in figure 4.13(c) shows a correctly located damage. The grey lines around the peak in 2.0m have a large spread. The big variations make the MSC untrustworthy. The removed bolts in figure 4.14(a) and (b) obtained peaks at x=2.0m, which makes the method unsatisfactory for boundary damages.

The numerical study did not obtain good results. Probably because of more pure bending modes in combination with a more sensitive behavior to small cut damages. Figure 4.15-4.18 show the results obtained from the numerical model, where the mode shapes are calculated from a modal analysis in ABAQUS. The cuts were modelled in the top web at x = {0.2m, 1.0m, 1.2m, 1.5m, 2.0m} with varying

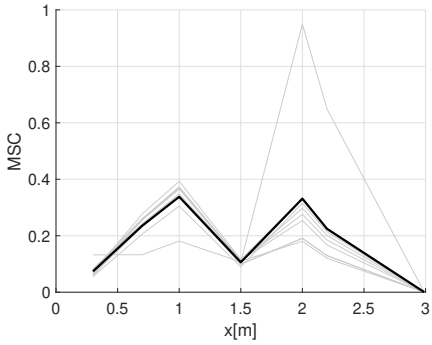

(a) First lateral mode of C70R40.

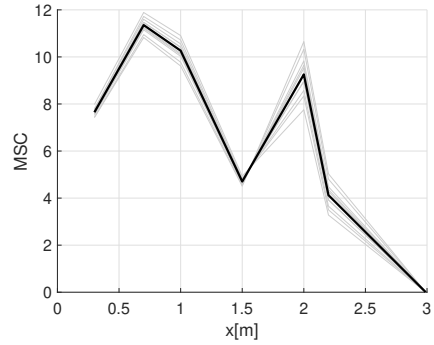

(b) First vertical mode of C70R40.

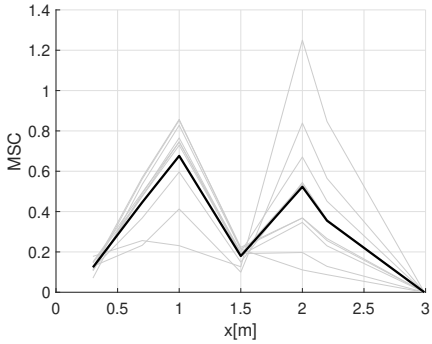

(c) First lateral mode of C70R70.

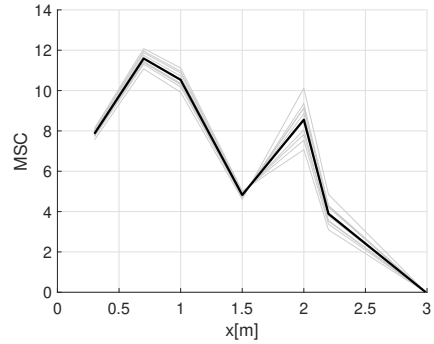

(d) First vertical mode of C70R70.

Figure 4.13: Experimental MSC of CR-damages.

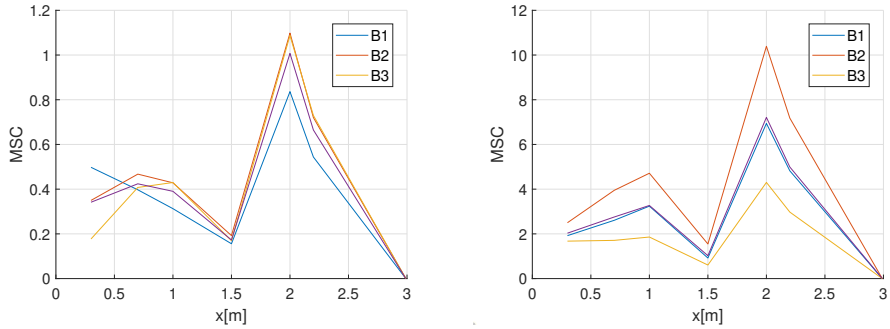

(a) First lateral mode. (b) First vertical mode.

Figure 4.14: Experimental MSC of B-damages.

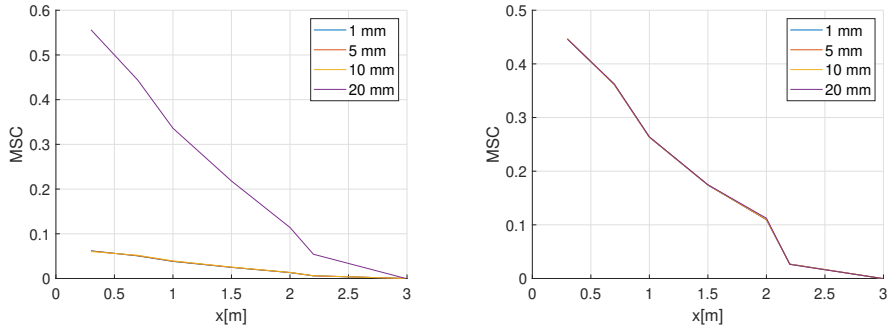

(a) First lateral mode. (b) First vertical mode.

Figure 4.15: Numerical MSC of cuts at (200, 0, 76).

deepness. The error peak in x=2.0m is observed for the lateral bending mode for the numerical model as in the experimental test, but the peak is not affecting the results in the vertical mode.
As examined in section 2.7.1, the Mode Shape Curvature method is originally designed for uniformly spaced sensors. Figure 4.19 shows the MSC for a numerical study modelled with uniformly spaced sensors of 10cm along the top web. The figure shows three different cuts of 10mm at different locations. The numerical MSC was based on the mean value of the first 24 modes obtained in the modal analysis, and the damages are perfectly located.

The Mode Shape Curvature is found by calculating the second derivative of the mode shape. When having non-uniformly sensor spacing there is a bigger error due to the central difference method. This, in combination with sensors placed at different webs and flanges, gives insufficient results. For the experimental tests the MSC feature did localize the deeper cuts, but it was first at 70mm that the damage was approximately located. This is close to the half of the cross-section height and

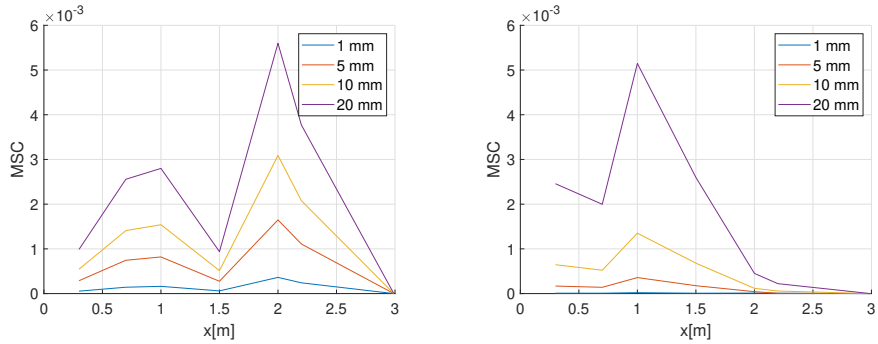

(a) First lateral mode. (b) First vertical mode.

Figure 4.16: Numerical MSC of cuts in (1200, 0, 76).

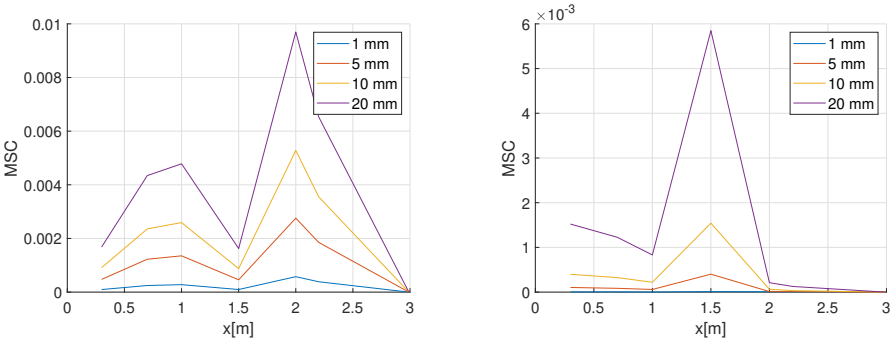

(a) First lateral mode. (b) First vertical mode.

Figure 4.17: Numerical MSC of cuts at (1500, 0, 76).

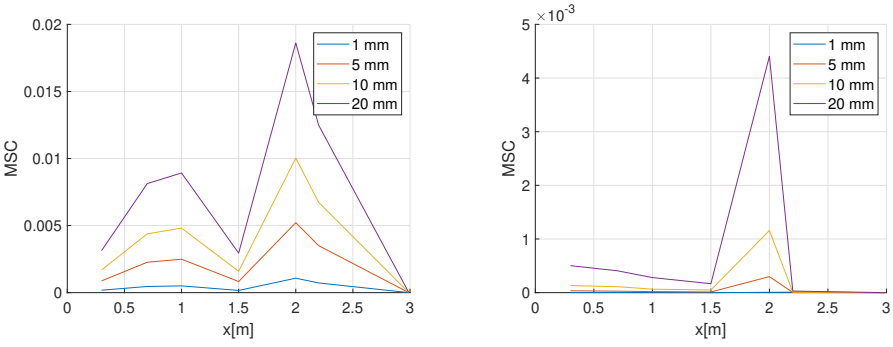

(a) First lateral mode. (b) First vertical mode.

Figure 4.18: Numerical MSC of cuts at (2000, 0, 76).

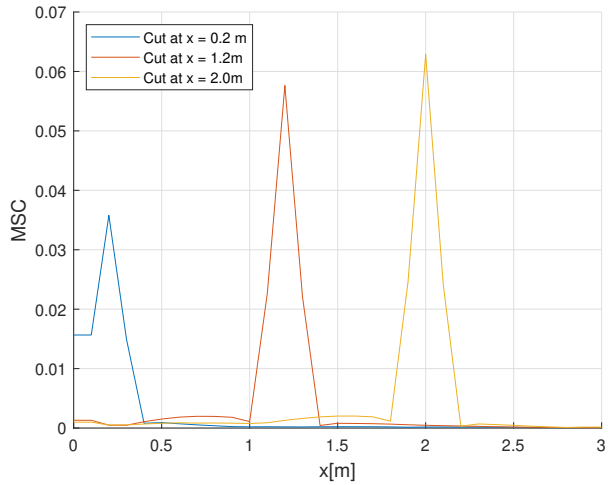

Figure 4.19: Numerical MSC for equally spaced sensors at the top web.

is considered as a severe damage. This makes the feature too insensitive in order to have a reliable structure. For pure bending modes as from the numerical study, 5mm cuts were detected and localized correctly, which is considered as a high degree of accuracy. Since the numerical study of uniformly spaced sensors along the top web gave good results, it would have been interesting to do an experimental test with equal sensor spacing in future work. It would also have been interesting to do an experiment with sensors along the top web with non-uniform spacing in order to identify whether the error was caused by the spacing or the varied mounting locations at the cross-section, i.e. mounting at different flanges and webs.

4.4 Modal Flexibility

Modal data from the system identifications of the damaged and undamaged cantilever were used to calculate the change in flexibility as given in equation (2.44). Flexibility changes, due to damages in the real-life cantilever, were calculated based on the average flexibility matrix. Meaning that the mean natural frequencies and average mode shapes were the basis for the calculation of the modal flexibility change. The modal average flexibility is given by:

$$[\overline{G}] \approx \sum_{i=1}^{m} \frac{1}{\overline{\omega}_i^2} \{\overline{\phi}\}_i \{\overline{\phi}\}_i^T. \tag{4.5}$$

The modal flexibility matrix converges as the modal frequency increases, therefore, only the first 7 modal contributions were used in the calculation of the modal flexibility change. The flexibility matrix was established by considering the translational degrees of freedom in both the transverse and vertical direction. Due to

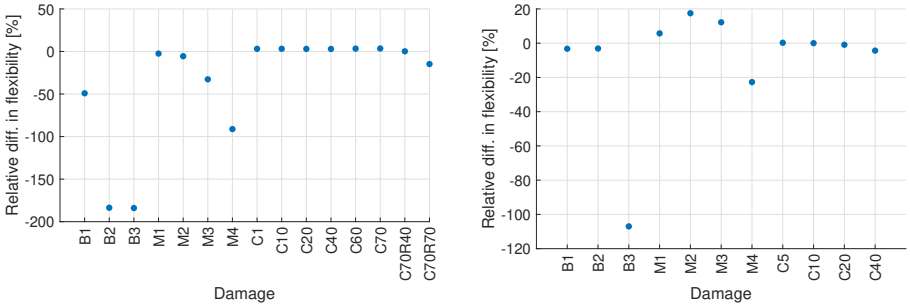

(a) Experimental damages (b) Numerical damages

Figure 4.20: Relative maximum modal flexibility change.

the mode reduction of some cut damages, mode 2 was excluded from the analysis for all damages. Figure 4.20(a) shows the relative maximum change in flexibility of the experimental damage scenarios. The relative maximum flexibility change for damage k is calculated as:

$$\Delta G_{max} = 100 \cdot \frac{G_{max,U} - G_{max,D_k}}{G_{max,U}}, \tag{4.6}$$

hence, $\Delta g_{max} < 0$ indicates an increase in flexibility. The removal of two bottom and side bolts caused the largest flexibility change of the real-life cantilever. The flexibility was increased by almost 200%. The point masses obtained an increasing flexibility for increasing damage level. The cut damages hardly affected the flexibility compared to the other two damages. It should be noted that the experimental and numerical flexibility results obtained quite different results. Figure 4.20(b) shows the absolute maximum change in flexibility of the numerical damages. The numerical flexibility change was calculated based on the modal parameters from the eigenvalue analysis. The removal of two bottom bolts resulted in the largest change of flexibility of the numerical damages. An interesting observation is how some point masses reduced the flexibility instead of increasing it. The modal flexibility method requires mass-normalized modes, which is difficult to obtain for experimental test. Therefore, the experimental mode shapes were normalized in such a way that the largest element in each mode shape vector was equal to unity.

The Modal Flexibility method could not locate damages in the cantilever beam. This is because the degrees of freedom are translational DOFs along the beam axis that gain stiffness from the structure as a whole. Thus, changes in flexibility in one of the DOFs cannot be linked to damage close to that degree of freedom. One must look at the pattern in the flexibility matrix and connect it to a pattern for a known damage. The flexibility change feature vector was established by rearranging the flexibility change matrix to row-vectors as:

$$\vec{d_1} = \begin{bmatrix} \Delta G_{*,1} & \Delta G_{*,2} & \dots & \Delta G_{*,N} \end{bmatrix}, \tag{4.7}$$

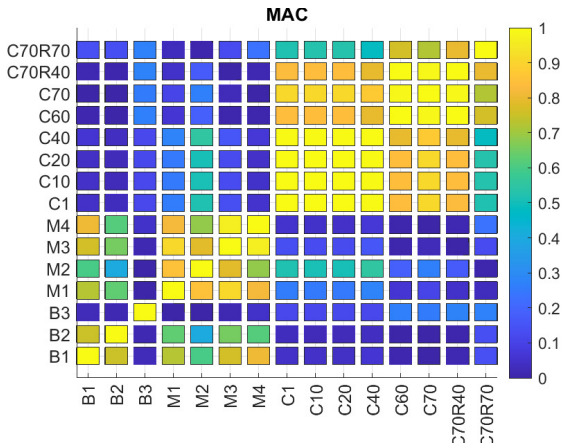

Figure 4.21: MAC matrix of modal flexibility change feature vectors.

where N is the number of sensors. Figure 4.21 shows the resulting MAC matrix of the modal flexibility change feature. The MAC matrix shows that the cut damages did not correlate with B- nor M-damages, while the latter two damages show signs of correlation. Also, the flexibility change feature vector of the B3 damage does not correlate with any other damage. In addition to the MAC matrix of the modal flexibility change, the flexibility feature vectors, given by:

$$\vec{d_2} = \begin{bmatrix} G_{*,1} & G_{*,2} & \dots & G_{*,N} \end{bmatrix}, \tag{4.8}$$

were evaluated by the damage index, DI. The damage index is the correlation coefficient between the damaged and undamaged cantilever beam, and is defined as [19]:

$$DI = 1 - \rho_{\vec{d}_D \vec{d}_U} = 1 - \frac{\sigma_{\vec{d}_U \vec{d}_D}}{\sigma_{\vec{d}_D} \sigma_{\vec{d}_U}} \tag{4.9}$$

where d_D and d_U are the feature vectors of the damaged and undamaged cantilever. $\sigma_{\vec{d}_D}$ and $\sigma_{\vec{d}_U}$ are the corresponding standard deviations, and $\sigma_{\vec{d}_U \vec{d}_D}$ is the covariance matrix. The damage indicator in equation (4.9) gives a non-dimensional measure of the similarity in the different damage behaviors. The damage indicator is low if the two feature vectors are similar, i.e. no presence of damage, and high if the vectors have a different behavior due to the presence of damage. Figure 4.22 shows the DI of the flexibility feature vectors as presented in equation (4.8) of the experimental damages. The figure shows the largest DI value for the B3 damage. The DI of the point mass damages increased as the point mass damage level increased. The different cut damages showed no trend for increased damage levels. The Modal Flexibility feature reached damage identification level (2). The method was successful in identifying severe damages, such as boundary damages and point masses, but could not locate damages in the structure. The use of the method to localize damages could not be justified for the sensor layout in this thesis. The

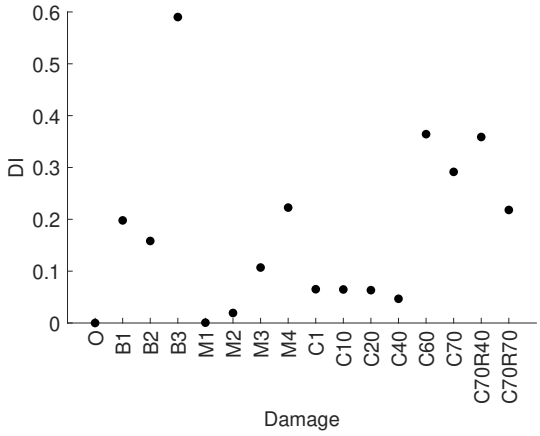

Figure 4.22: Damage Index of modal flexibility feature vectors.

method has been applied successfully for damage identification in studies evaluating other shell models [15, 21]. Shell models can easily relate the flexibility matrix to a location in the model, while in the case of this thesis, the degrees of freedom obtained flexibility change from the global stiffness. The numerical damages were most likely located at the tip, since the stiffness on the tip of the cantilever depends on the stiffness of the entire beam.

The flexibility matrix was estimated by equation (2.43), which is based on the natural frequency and mode shape estimates. Damages that cause a reduction in natural frequencies are a result of either a stiffness reduction or an increase in mass. Since most of the damages evaluated in this thesis reduced the natural frequencies, the flexibility of the damaged system increased. The removal of two bottom bolts resulted in the largest frequency shift, and the largest flexibility change was recorded for the B3 damage in both studies. Furthermore, the removal of two side bolts caused a large change in the flexibility. Both damages obtained a much higher flexibility compared to removing one single bolt. The experimental study showed an increasing trend when increasing from the B1 boundary damage level to B2 and B3.

The numerical study was investigated for mass normalized mode shapes, as the method requires. The experimental study was evaluated for mode shapes normalized by the maximum entry in each mode shape. The two different methods of normalization may be the reason for the slightly different results. The flexibility change of the experimental mass damages showed an increasing trend as the point mass damage level increase. This pattern cannot be seen for the numerical point mass damages, as the largest point mass measures a significant flexibility change. The cut damages experienced quite different behaviors for the finite element model and the real-life cantilever. The numerical results showed that the maximum flexibility change increased with increasing cut depth in x=0.2m, while a decreasing trend could be observed for constant cut depth of 20mm with increasing distance

from the support. The global stiffness will be higher as the cut occurs further away from the support, since a larger part of the structural beam remains undamaged. The experimental study could not have been performed with cuts at different locations, as only one test piece was available. The maximum change in flexibility remained relatively constant for the lower cut damage levels (C1-C40). The cut damages did not show any monotonic trends, indicating that the maximum flexibility change was not a good feature for cut damages. The largest cut damages C60, C70 and C70R40 recorded only 17 modes, which caused difficulties when applying the Modal Flexibility method. Based on the results from the natural frequency and mode shape analyzes, it was decided to exclude the second mode from all damages in the analysis. Some damages cause modes to shift, therefore the second mode could have been important for the flexibility calculations.

Based on the flexibility results presented in this section, the flexibility will be a good damage indicator for damages causing large frequency shifts, such as B-damages and large M-damages. The method gave inconsistent results for the experiments and the numerical model. It is reemphasized that the normalization of mode shapes play an important role in the flexibility estimations. It is proposed as future work to evaluate if the method obtains better results if the experimental mode shapes are mass-normalized, and the numerical flexibility based on FDD estimated modal parameters instead of the eigenvalue results.

4.5 Statistical Moments

Statistical moments can give statistical information about the acceleration response histories. The peak amplitude, mean, root-mean square, variance, skewness and kurtosis given in table 2.1, were used to characterize the irregular response of the beam. Vertical acceleration responses recorded by the sensor at the tip are shown in figure 4.23. The figure clearly shows that the applied loads varies in magnitude and duration, which is due to the use of tapping as load. Statistical moments as damage feature were first evaluated for the white noise intervals. Each 5-minute recording includes 60 seconds of white noise response at the beginning and end of the response history. 10 seconds were removed from the start and end of both intervals in order to remove deviations resulting from human errors. In order to ensure that only white noise signals were included, the intervals evaluated were: 10-50 seconds and 270-300 seconds. The last interval was reduced so that the vibration due to the third applied load would have stabilized.

Statistical moments were calculated for each time series, and due to a large spread in the experimental data, in addition to a low number of tests, a mean value was established for each sensor for each damage. Figure 4.24(a)-(f) shows the statistical moments of sensor A00z for the interval from 10 to 50 seconds. A00z was investigated due to the assumption that the sensor would experience the largest acceleration amplitudes. Figure 4.25(a)-(f) shows the statistical moments of the time interval from 270 to 300 seconds.

The peak amplitude statistic differentiates between the two white noise intervals. The largest peak amplitude of the first interval was obtained for the B3

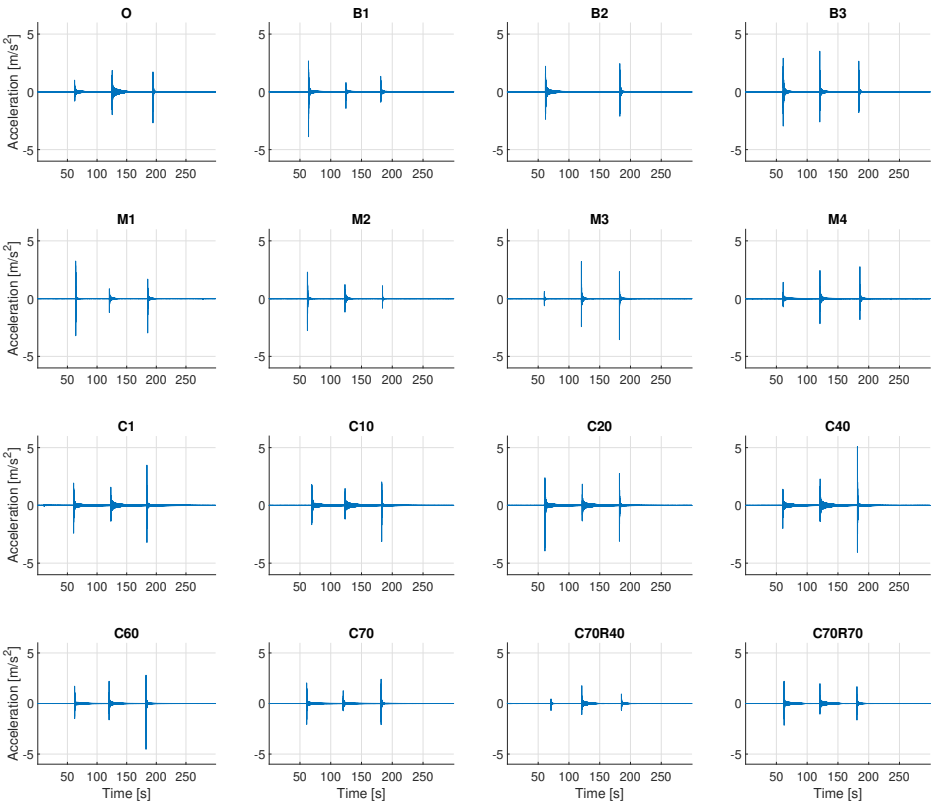

Figure 4.23: Response time-histories of sensor A00z.

damage, while the second time interval recorded largest peak amplitude of the B1 damage, as shown in figure 4.24(a) and 4.25(a). Figure 4.24(b) and 4.25(b) show a significant increase in mean acceleration when a damage was present. The boundary and cut damages obtained approximately the same mean. However, the mean slightly increases as the cut depth increased. The largest mean acceleration was obtained for the M-damages, except from M4 in both cases. The root-mean square and variance values are shown in figure 4.24(c)-(d) and 4.25(c)-(d). The largest root-mean square (RMS) was recorded for the M4 damage, and the RMS and variance were increasing as the point mass damage level increased. The B-damages resulted in approximately the same RMS as the undamaged beam, where the B1 damage deviated the most. Both figures show an overall decreasing pattern when the cut depth increase.

The skewness of a Gaussian distributed variable, such as white noise, is approximately 0, while the kurtosis is approximately 3. Figure 4.24(f) and 4.25(f) show two deviations. The B3-damage slightly deviates from the zero-line in figure 4.24(e), while M1 recorded a larger negative skewness for the second time interval in figure 4.25(e). The damages with skewness-deviations also obtained large kurtosis

values. These large values might have been caused by signal errors in the vibration recording from the white noise load. The statistical moments in figure 4.24 and 4.25 show no clear tendencies besides the increasing mean due to the presence of damage.

The statistical features of the load-intervals are shown in figure 4.26(a)-(f). The beam was put in vibration by tapping the tip of the beam. Therefore, the peak acceleration is a very sensitive parameter when the applied load is inconsistent. The peak amplitude will typically increase when a damage reduces the structural stiffness. This only applies when the input to the system remains stationary, which was not the case in this thesis. Therefore, the peak amplitude was not a good indicator for the acceleration response histories. The variance, skewness and kurtosis

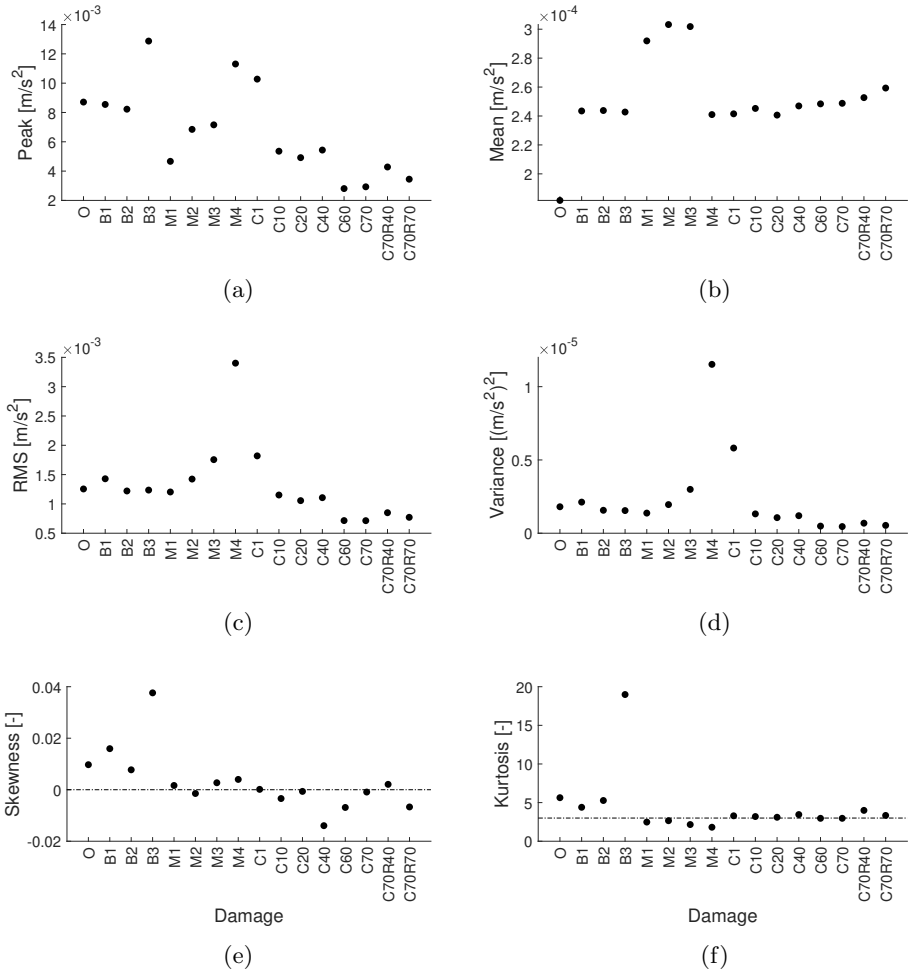

Figure 4.24: Statistical moments of white noise interval from 10-50s (sensor A00z).

produce biased estimates of the statistics. This is a possible error, as there were not sufficient acceleration history recordings of the damages [6]. Thus, neither of these features would be good indicators for the acceleration response histories. The mean acceleration values show somewhat similar trends as the means of the white noise intervals. The load response history also indicates the presence of damage by an increase in the mean acceleration. The mean of the largest point mass did not increase as much as the other M-damages. The mean value is sensitive to outliers which can be the reason for this effect. Since the median is a statistic similar to the mean value, but less sensitive to outliers, this could be a better feature. The mean value is a statistic that successfully indicated if the structure was

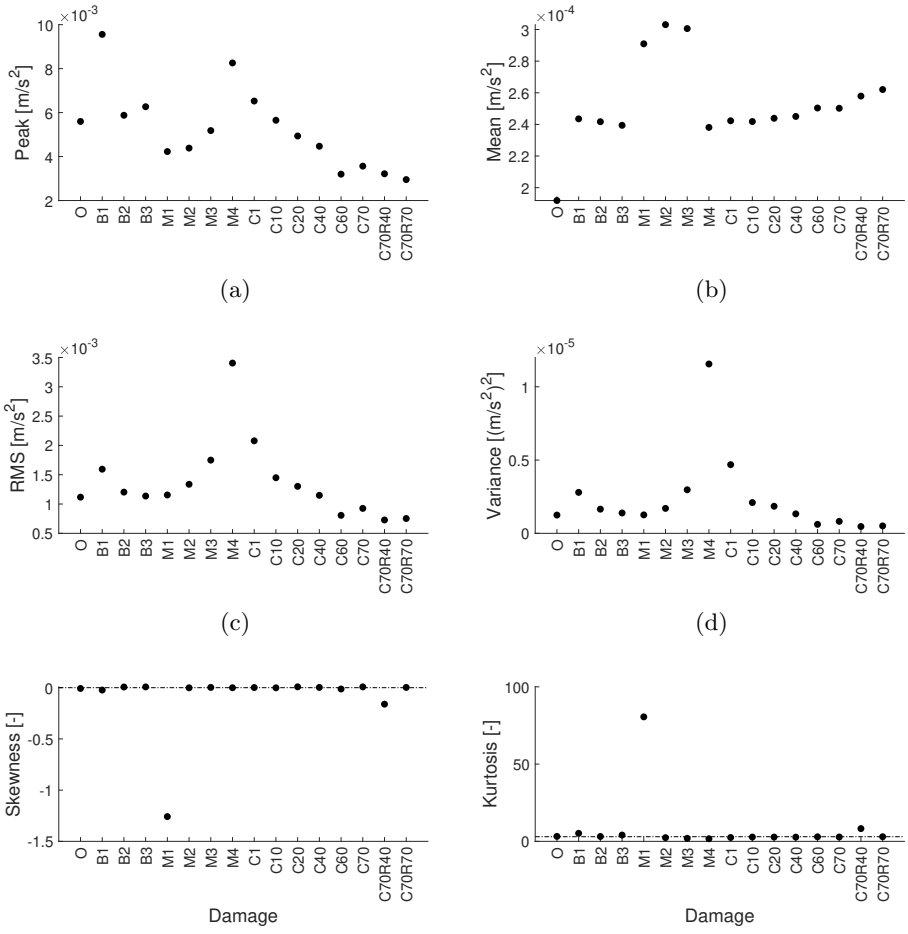

Figure 4.25: Statistical moments of white noise interval from 270-300s (sensor A00z).

subjected to damage, but could not be used to separate the different B-, M-, C- and CR-damages. The other statistical moments in figure 4.26(c)-(f) show a large dispersion between the statistics of the different loads. An interesting observation was how the root-mean square of some damage levels were lower than root-mean square of the undamaged beam. The mean spectral density of the C-damaged beam subjected to a vertical load, is shown in figure 4.27. The first peak around 8.8Hz shows that for C1-C40 the energy associated with the mode increased when the C-damages were present. an interesting observation was that the C60 and C70 damages measured less energy in the system than the undamaged beam. The other peaks around 26.3Hz, 43.8Hz, 55.6Hz and 61.5Hz show that the cuts tend to reduce

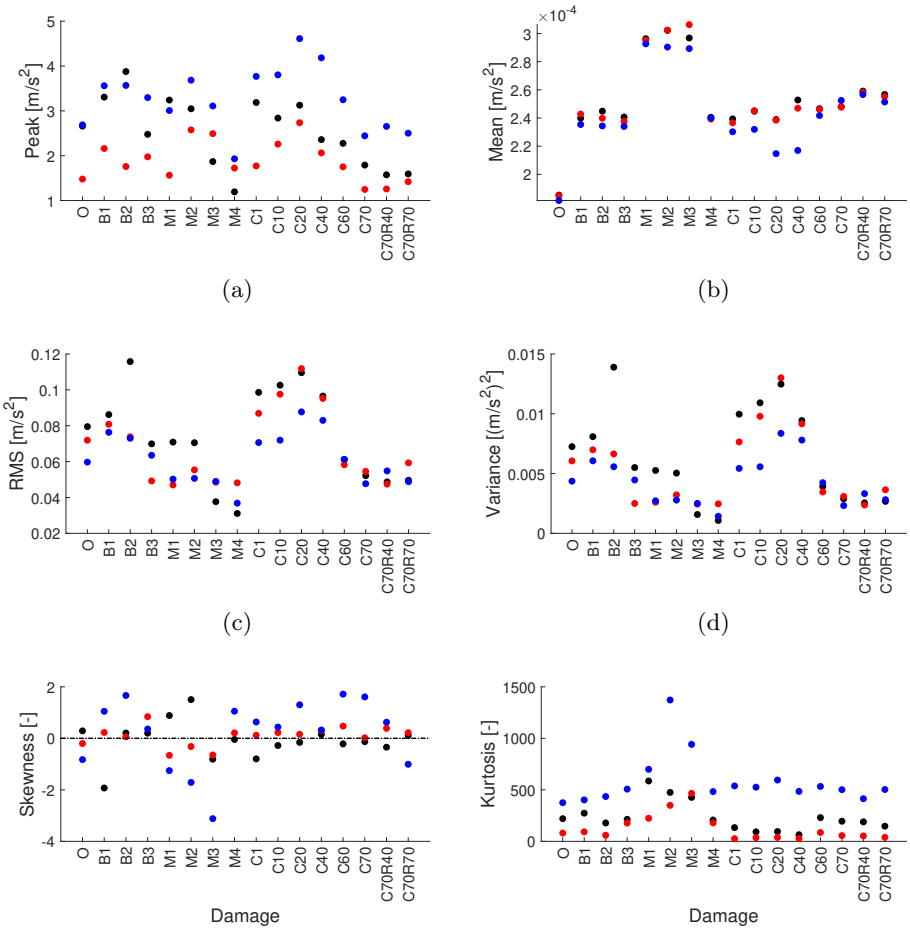

Figure 4.26: Statistical moments of load intervals: ● vertical tap flange , ● vertical tap web and ● horizontal tap web (sensor A00z).

the amount of energy associated with the mode. The second peak shows a quite large reduction in the peak, still there are no obvious trends in the reduction. The higher order modes from the peak around 133.8Hz shows that the energy in the undamaged structure was less than the lower cut damage levels. The figure shows that as the cut depth increased, the two peaks around 142Hz to 152Hz merged and shifted slightly to the left.

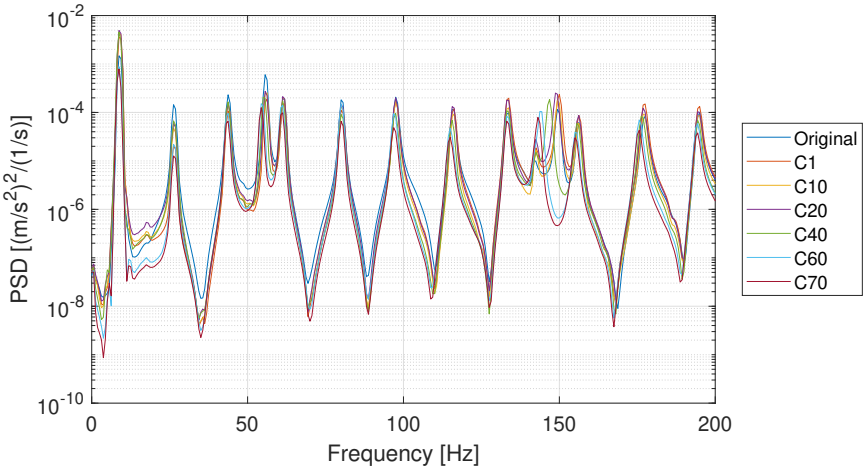

Figure 4.27: Average power spectral density of cut damages for 60-120s load interval (sensor A00z).

The root-mean square shows no clear tendencies for either the white noise intervals and the load intervals. The root-mean square acceleration gives information about the energy in the system, and the power spectral density gives information about the energy in the context of frequency. The power spectral density of the first recorded peak shows that all cut damages reduced in energy related to the mode. The recorded spectral density of the C60 and C70 damages were lower than the undamaged beam, while higher for the lower cut damages. The spectral densities neither showed any clear trends for the spectral density peaks. Thus, a reasonable explanation was not found for why some damages obtained lower RMS estimations than the undamaged beam. The root-mean square will therefore not be a good damage feature. The variance also measures spread of data about the mean value of the acceleration amplitudes. Variance obtain very similar patterns to the root-mean square.

The symmetry of the probability distribution of the response history was evaluated in terms of skewness. The Gaussian distributed white noise acceleration histories obtained skewness close to zero. The recorded deviations were a result of error in the recorded signal as well as small vibration amplitudes of the beam. The skewness of the load response series obtained much larger skewness magnitudes. The skewness did not indicated any reasonable trend for the increased damage levels. This also applied for the kurtosis. 10 recordings were proven insufficient in

order to obtain good statistical results and may illuminate trends that exist.

The statistical moments can give more information about the damage if the statistical moments are formed as a feature vector:

$$\vec{d} = [\vec{y}_{peak} \quad \vec{\overline{y}} \quad \vec{RMS} \quad \vec{\sigma^2} \quad \vec{\gamma} \quad \vec{\kappa}], \tag{4.10}$$

where each statistical moment vector within $\vec{d}$ consists of average values of all sensors. The peak amplitude feature vector of a given damage is:

$$\vec{y}_{peak,D} = [y_{peak,s1} \quad y_{peak,s2} \quad \cdots \quad y_{peak,s14}], \tag{4.11}$$

where the peak values of each sensor are the average value of the 10 test for damage D. The remaining vectors in equation (4.10) were established like the peak amplitude in equation (4.11). Figure 4.28(a) shows the DI values of the feature vector in equation (4.10) for the three load intervals. The feature vectors show much higher DI values for the vertical loads than the lateral. Due to the sensitive and bias behavior of the recordings, the peak amplitude, variance, skewness and kurtosis were excluded. The DI of the resulting feature vector is shown in figure 4.28(b). The largest DI values were obtained for the higher point mass damage levels. Still, the different loads showed no clear tendencies.

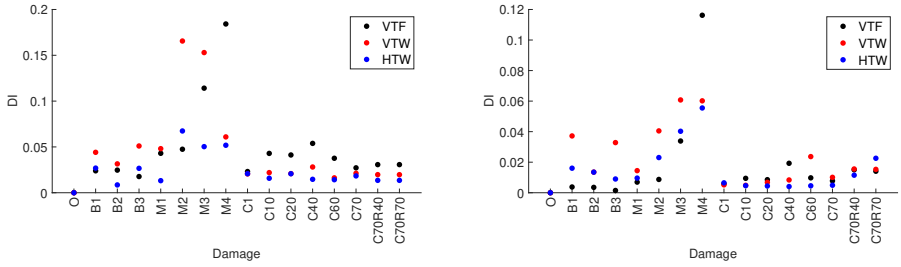

(a) All statistical moments

(b) $\overline{y}$, RMS

Figure 4.28: Damage index of different statistical moment feature vectors of load intervals.

The entire response histories from 0 to 300 seconds were also evaluated by the two statistical moment feature vectors. The time interval shows little variation in the DI of the different feature vectors, as shown in figure 4.29. Both feature vectors obtained an increasing DI for increasing point mass damages. As the sensitive moments were excluded, the point mass damage separates more from the other damages. It should be noted that the DI magnitude heavily decreased as the variance, skewness and kurtosis were excluded. Figure 4.29 indicates that higher point mass damages could be separated by statistical moments when the entire response history was evaluated. Since the feature vectors of the load intervals show no trends, the strength of the statistical moment feature vectors is weakened. A future study should include a larger number of samples, in addition to evaluating the statistical moments for consistent loading.

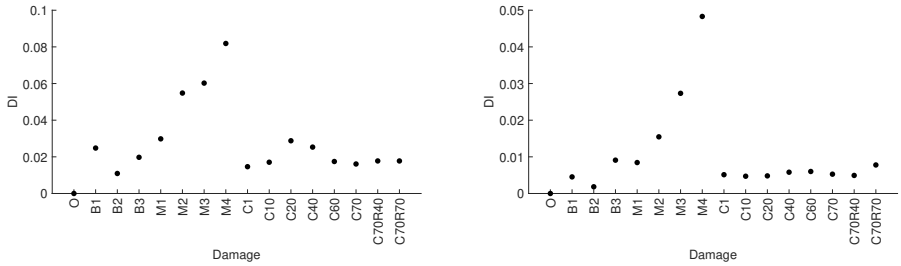

(a) All statistical moments

(b) $\overline{y}$, RMS

Figure 4.29: Damage index of different statistical moment feature vectors of 5-minute response histories.

Chapter 5

Conclusion

Based on acceleration measurements of numerical and experimental studies, the simplest damage features, such as natural frequencies and mode shapes, are proven to be the most sufficient in detecting damages. These are the only damage features proven to work correctly in this thesis, and will also give good results for real-life structures. The results show that cut damages must have been at least 40mm deep in order to detect the damage. This is a severe damage compared to the dimensions of the structure and should be detected way earlier in order to have a comfortable and reliable structure. The modal flexibility combines the natural frequencies and mode shapes into one feature. The modal flexibility feature will estimate damages causing large frequency shifts, but will not classify the damage type. Thus, the natural frequency shifts, mode shapes and modal flexibility features reach damage identification level (3). None of the methods manages to locate the damage.

The mode shape curvature suffers from the sensor layout limitations, but did manage to localize cuts of 70mm. The numerical results show that the mode shape curvature method was successfully applied for cut damages when a larger number of sensors were used, and the spacing between the sensors was uniform. The statistical moments were proven insufficient for damage identification. From the statistical moment analysis, only the mean value showed a consistent increase for all damages. The mean acceleration feature should be questioned as the smallest cut damage and the largest point mass damage indicates equal shifts.

In addition to presenting which damage indicators that are reliable, the thesis has presented typical trends of the different damage types for the different features.

Bibliography

[1] M. Allen, R. L. Mayers, and D. Rixen. *Dynamics of Coupled Structures*, volume 4 of *Conference Proceedings of the Society for Experimental Mechanics*. Springer, 2016. ISBN 978-3-319-29762-0.

[2] D. G. Altman, D. Machin, T. N. Bryant, and M. J. Gardner. *Statistics with Confidence: Confidence Intervals and Statistical Guidelines*. BMJ Books, 2 edition, 2000. ISBN 978-0-7279-1375-3.

[3] I. Chowdhury and S. Dasgupta. Computation of Rayleigh Damping Coefficients for Large Systems. *Int. J. Space Struct.*, 43:6855–6868, Jan. 2003.

[4] G. B. Coleman and H. c. Andrews. Image segmentation by clustering. *Proceedings of the IEEE*, 67(5):773–785, May 1979. doi: 10.1109.

[5] M. Döhler, F. Hille, L. Mevel, and W. Rücker. Structural health monitoring with statistical methods during progressive damage test of S101 Bridge. *Engineering Structures*, 69:183–193, June 2014. doi: 10.1016/j.engstruct.2014.03.010.

[6] C. R. Farrar and K. Worden. *Structural Health Monitoring*. Wiley, Chichester, 2013. ISBN 978-1-119-99433-6.

[7] J. R. Fjelldal. Modelling and Dynamic Behavior of Hell Bridge Test Arena. Technical report, NTNU (Norwegian University of Science and Technology), Faculty of Engineering, Department of Structural Engineering, Trondheim, Dec. 2019.

[8] G. T. Frøseth. *Load model of historic traffic for fatigue life estimation of Norwegian railway bridges*. NTNU, 2019. ISBN 978-82-326-3749-2. Accepted: 2019-07-10T15:34:49Z ISSN: 1503-8181.

[9] S. Gopalakrishnan, M. Ruzzene, and S. Hanagud. *Computational Techniques for Structural Health Monitoring*. Springer Series in Reliability Engineering. Springer, London, 2011. ISBN 978-0-85729-283-4.

[10] S. Greenland, S. J. Senn, and K. J. Rothman. Statistical tests, P values, confidence intervals, and power: a guide to misinterpretations. May 2016.

[11] M. Holický. *Introduction to Probability and Statistics for Engineers*. Springer Science & Business Media, Aug. 2013. ISBN 978-3-642-38300-7.

[12] A. M. Kjøle. Modelling and Dynamic Behavior of Hell Bridge Test Arena. Technical report, NTNU (Norwegian University of Science and Technology), Faculty of Engineering, Department of Structural Engineering, Trondheim, Dec. 2020.

[13] C. G. Koh, G. Q. Qiao, and S. T. Quek. Damage Identification of Structural Members: Numerical and Experimental Studies. *Structural Health Monitoring*, 2(1):41–55, Mar. 2003. doi: 10.1177/147592103031112. Publisher: SAGE Publications.

[14] D. E. Newland. *An Introduction to Random Vibrations, Spectral & Wavelet Analysis*. Dover Publications, 3 edition, 2005. ISBN 978-0-486-44274-7.

[15] A. K. Pandey and M. Biswas. Damage Detection in Structures Using Changes in Flexibility. *Journal of Sound and Vibration*, 169(1):3–17, Jan. 1994. doi: 10.1006/jsvi.1994.1002.

[16] A. K. Pandey, M. Biswas, and M. M. Samman. Damage detection from changes in curvature mode shapes. *Journal of Sound and Vibration*, 145(2):321–332, Mar. 1991. doi: 10.1016/0022-460X(91)90595-B.

[17] C. Rainieri and G. Fabbrocino. *Operational Modal Analysis of CivilEngineering Structures: An Introduction and Guide for Applications*. Springer New York, 2014. ISBN 978-1-4939-0766-3.

[18] N. Sfakianakis. *Finite Difference schemes on non-Uniform meshes for Hyperbolic Conservation Laws*. PhD thesis, University of Crete, Heraklion, Feb. 2009.

[19] B. T. Svendsen, G. T. Frøseth, and A. Rönnquist. Damage Detection Applied to a Full-Scale Steel Bridge Using Temporal Moments. *Shock and Vibration*, 2020:3083752, Feb. 2020. ISSN 1070-9622. doi: 10.1155/2020/3083752. Publisher: Hindawi.

[20] M. Tarpø, P. Olsen, S. Amador, M. Juul, and R. Brincker. On minimizing the influence of the noise tail of correlation functions in operational modal analysis. *Procedia Engineering*, 199:1038 – 1043, 2017.

[21] J. Zhao and J. T. DeWolf. Sensitivity Study for Vibrational Parameters Used in Damage Detection. *Journal of Structural Engineering*, 125(4):410–416, Apr. 1999. doi: 10.1061/(ASCE)0733-9445(1999)125:4(410).

Appendix A

Table A1: Natural frequencies obtained from FDD of numerical model with 7 sensors. MAC and relative error with results from eigenvalue analysis of FE model.

Mode no.	**Frequency FEM [Hz]**	**Frequency FDD [Hz]**	**MAC**	**Relative Error [%]**
1	8.31	8.33	0.93	0.32
2	8.50	8.57	0.99	0.75
3	9.35	9.35	0.63	0.06
4	25.72	25.71	1.00	0.07
5	43.00	42.88	1.00	0.27
6	53.33	53.09	1.00	0.45
7	57.95	57.59	1.00	0.62
8	60.47	60.06	1.00	0.68
9	78.20	77.27	1.00	1.19
10	96.27	94.45	1.00	1.19
11	114.76	111.66	1.00	2.70
12	133.72	128.84	1.00	3.65
13	147.03	140.61	1.00	4.36
14	153.25	146.25	0.94	4.57
15	155.25	148.40	0.63	4.83
16	173.39	163.11	0.99	5.93
17	194.23	180.09	1.00	7.28
18	215.84	197.00	1.00	8.73
19	238.27	213.66	1.00	10.33
20	261.62	231.54	0.78	11.50
21	261.75			
22	270.75	235.54	0.93	13.00
23	286.96	246.33	0.98	13.86
24	311.36	262.69	0.98	15.63
25	337.91	281.62	0.01	16.66
26	340.82	301.62	0.01	11.47
27	345.16	324.07	0.09	6.11
28	365.71	337.14	0.01	7.81

Table A2: Description of time series for boundary damages.

Damage	**Filename**	**Length of time series [s]**	**Sensor placement**
No damage	2020-04-30-08-53-15Z	306.8	See fig. 3.5
	2020-04-30-09-01-36Z	325.1	
	2020-04-30-09-07-06Z	335.3	
	2020-04-30-09-12-52Z	304.1	
	2020-04-30-09-18-12Z	302.7	
	2020-04-30-09-23-26Z	302.0	
	2020-04-30-09-35-47Z	303.9	
	2020-03-12-1	310.8	
	2020-03-12-2	353.1	
	2020-03-12-3	303.1	
B1	2020-05-04-07-52-00Z	303.6	See fig. 3.5
	2020-05-04-07-07-15Z	313.6	
	2020-05-04-08-02-40Z	307.6	
	2020-05-04-08-08-06Z	307.2	
	2020-05-04-08-13-29Z	304.1	
	2020-05-04-08-18-40Z	303.1	
	2020-05-04-08-23-53Z	304.1	
	2020-05-04-08-29-10Z	307.2	
	2020-05-04-08-34-40Z	301.7	
	2020-05-04-08-39-56Z	303.8	
B2	2020-05-04-09-02-25Z	305.6	See fig. 3.5
	2020-05-04-09-08-57Z	304.0	
	2020-05-04-09-14-17Z	303.2	
	2020-05-04-09-19-32Z	301.8	
	2020-05-04-09-24-47Z	414.9	
	2020-05-04-09-32-01Z	302.7	
	2020-05-04-09-37-16Z	301.7	
	2020-05-04-09-42-26Z	300.6	
	2020-05-04-09-47-35Z	311.3	
	2020-05-04-09-53-02Z	304.7	
B3	2020-05-04-10-22-02Z	323.8	See fig. 3.5
	2020-05-04-10-27-37Z	303.9	
	2020-05-04-10-32-53Z	303.3	
	2020-05-04-10-38-26Z	302.7	
	2020-05-04-10-43-40Z	304.2	
	2020-05-04-10-48-53Z	303.1	
	2020-05-04-10-54-08Z	301.9	
	2020-05-04-10-59-28Z	302.9	
	2020-05-04-11-04-40Z	302.3	
	2020-05-04-11-09-56Z	300.8	

Table A3: Description of time series for point mass.

Damage	**Filename**	**Length of time series [s]**	**Sensor placement**
M1	2020-05-04-10-22-02Z	300.8	See fig. 3.5
	2020-04-30-10-38-36Z	303.8	
	2020-04-30-10-44-04Z	312.1	
	2020-04-30-10-49-26Z	306.8	
	2020-04-30-10-55-06Z	305.9	
	2020-04-30-11-00-29Z	304.4	
	2020-04-30-11-05-45Z	304.2	
	2020-04-30-11-11-00Z	305.2	
	2020-04-30-11-16-18Z	320.5	
	2020-04-30-11-21-29Z	305.3	
M2	2020-04-30-11-26-58Z	305.3	See fig. 3.5
	2020-04-30-11-42-56Z	308.7	
	2020-04-30-11-48-13Z	315.0	
	2020-04-30-11-53-31Z	301.9	
	2020-04-30-11-58-57Z	328.9	
	2020-04-30-12-04-14Z	302.4	
	2020-04-30-12-09-52Z	310.2	
	2020-04-30-12-15-00Z	310.2	
	2020-04-30-12-20-21Z	303.4	
	2020-04-30-12-25-41Z	302.8	
M3	2020-04-30-12-39-20Z	304.3	See fig. 3.5
	2020-04-30-12-44-32Z	302.7	
	2020-04-30-12-49-47Z	306.0	
	2020-04-30-12-55-04Z	302.5	
	2020-04-30-13-00-14Z	302.5	
	2020-04-30-13-05-26Z	301.4	
	2020-04-30-13-10-35Z	305.3	
	2020-04-30-13-15-53Z	300.8	
	2020-04-30-13-21-05Z	306.9	
	2020-04-30-13-26-18Z	306.9	
M4	2020-05-04-06-46-05Z	306.4	See fig. 3.5
	2020-05-04-06-51-24Z	303.4	
	2020-05-04-06-56-37Z	303.4	
	2020-05-04-07-01-50Z	303.5	
	2020-05-04-07-07-05Z	302.5	
	2020-05-04-07-12-32Z	302.9	
	2020-05-04-07-17-46Z	300.7	
	2020-05-04-07-22-59Z	328.0	
	2020-05-04-07-28-50Z	304.3	
	2020-05-04-07-34-06Z	303.1	

Table A4: Description of time series for C1-C40.

Damage	**Filename**	**Length of time series [s]**	**Sensor placement**
C1	2020-05-04-11-38-09Z	302.3	See fig. 3.5
	2020-05-04-11-43-26Z	308.8	
	2020-05-05-07-27-37Z	302.9	
	2020-05-05-07-32-51Z	304.3	
	2020-05-05-07-38-05Z	302.1	
	2020-05-05-07-43-19Z	302.0	
	2020-05-05-07-48-30Z	302.4	
	2020-05-05-07-53-44Z	304.0	
	2020-05-05-07-59-01Z	307.5	
	2020-05-05-08-12-39Z	301.5	
C10	2020-05-05-08-24-23Z	306.5	See fig. 3.5
	2020-05-05-08-29-42Z	304.0	
	2020-05-05-08-35-00Z	303.6	
	2020-05-05-08-40-12Z	303.2	
	2020-05-05-08-45-31Z	302.7	
	2020-05-05-08-50-42Z	310.2	
	2020-05-05-08-55-59Z	303.8	
	2020-05-05-09-01-11Z	302.7	
	2020-05-05-09-06-31Z	304.4	
	2020-05-05-09-11-46Z	305.1	
C20	2020-05-05-09-21-11Z	302.6	See fig. 3.5
	2020-05-05-09-29-09Z	303.2	
	2020-05-05-09-34-21Z	302.5	
	2020-05-05-09-39-34Z	304.6	
	2020-05-05-09-44-48Z	306.3	
	2020-05-05-09-50-13Z	305.1	
	2020-05-05-09-55-32Z	302.4	
	2020-05-05-10-00-43Z	303.2	
	2020-05-05-10-05-57Z	303.0	
	2020-05-05-10-11-11Z	302.7	
C40	2020-05-05-10-20-27Z	324.7	See fig. 3.5
	2020-05-05-10-26-08Z	303.1	
	2020-05-05-10-31-20Z	302.7	
	2020-05-05-10-36-32Z	302.0	
	2020-05-05-10-57-00Z	300.8	
	2020-05-05-11-02-17Z	300.4	
	2020-05-05-11-07-29Z	307.3	
	2020-05-05-11-12-47Z	304.7	
	2020-05-05-11-18-04Z	313.0	
	2020-05-05-11-23-34Z	307.1	

Table A5: Description of time series for C60-C70R70.

Damage	**Filename**	**Length of time series [s]**	**Sensor placement**
C60	2020-05-22-09-19-47Z	301.1	See fig. 3.5
	2020-05-22-09-25-13Z	303.1	
	2020-05-22-09-34-57Z	301.7	
	2020-05-22-09-40-10Z	304.5	
	2020-05-22-09-45-23Z	302.8	
	2020-05-22-09-50-35Z	305.6	
	2020-05-22-09-56-28Z	302.2	
	2020-05-22-10-01-41Z	304.0	
	2020-05-22-10-07-04Z	304.9	
	2020-05-22-10-12-21Z	304.4	
C70	2020-05-22-10-53-34Z	302.0	See fig. 3.5
	2020-05-22-10-58-55Z	302.2	
	2020-05-22-11-04-06Z	304.7	
	2020-05-22-11-09-23Z	304.0	
	2020-05-22-11-14-36Z	302.0	
	2020-05-22-11-21-29Z	314.7	
	2020-05-22-11-29-28Z	304.5	
	2020-05-22-11-34-47Z	303.9	
	2020-05-22-11-40-02Z	303.4	
	2020-05-22-11-45-23Z	300.9	
C70R40	2020-05-22-11-59-27Z	301.6	See fig. 3.5
	2020-05-22-12-04-41Z	300.8	
	2020-05-22-12-09-52Z	301.3	
	2020-05-22-12-15-02Z	303.0	
	2020-05-22-12-20-15Z	303.3	
	2020-05-22-12-25-38Z	301.5	
	2020-05-22-12-32-12Z	303.8	
	2020-05-22-12-39-50Z	303.9	
	2020-05-22-12-45-05Z	301.2	
	2020-05-22-12-50-32Z	302.5	
C70R70	2020-05-22-13-02-18Z	305.8	See fig. 3.5
	2020-05-22-13-07-38Z	300.5	
	2020-05-22-13-12-48Z	301.7	
	2020-05-22-13-17-58Z	304.6	
	2020-05-22-13-23-13Z	300.5	
	2020-05-22-13-28-25Z	300.4	
	2020-05-22-13-33-36Z	302.7	
	2020-05-22-13-38-49Z	300.7	
	2020-05-22-13-44-00Z	302.0	
	2020-05-22-13-49-15Z	303.2	

Table A6: Percentiles for the undamaged beam.

Mode	5%	95%	**Mode**	5%	95%
1	7.89	7.91	10	97.50	97.60
2	8.81	8.83	11	115.93	116.03
3	9.03	9.05	12	133.30	133.40
4	26.45	26.47	13	141.49	141.64
5	43.78	43.82	14	149.43	149.62
6	50.86	50.89	15	156.31	156.36
7	55.77	55.81	16	177.20	177.31
8	61.53	61.62	17	194.79	194.88
9	80.24	80.28	18	211.37	211.60

Table A7: Max and min frequencies for point masses.

Mode	M1		M2		M3		M4	
	5%	95%	5%	95%	5%	95%	5%	95%
1	7.79	7.82	7.69	7.74	6.82	6.83	5.96	5.97
2	8.68	8.70	8.55	8.55	7.45	7.47	6.67	6.67
3	8.96	8.98	8.93	8.96	8.81	8.82	8.62	8.63
4	26.21	26.29	26.08	26.10	24.39	24.46	22.98	23.09
5	43.22	43.34	42.97	43.04	39.54	39.71	37.28	37.76
6	50.16	50.20	49.62	49.64	46.55	46.57	44.19	44.54
7	55.03	55.23	54.47	54.49	51.56	51.58	50.28	50.31
8	60.99	61.12	60.61	60.63	58.74	58.80	57.58	57.71
9	79.78	79.84	79.18	79.22	75.87	76.02	74.69	74.86
10	96.91	96.95	96.20	96.23	92.27	93.67	90.51	92.06
11	115.33	115.41	114.74	114.79	110.80	112.86	107.90	109.10
12	132.36	132.39	131.14	131.31	123.99	126.84	123.60	125.92
13	138.80	139.07	137.60	138.78	128.61	129.83	127.40	128.10
14	147.68	147.76	145.38	145.70	141.01	141.19	139.40	140.01
15	154.97	155.03	154.38	154.46	152.94	153.35	150.00	152.30
16	176.06	176.16	175.22	175.50	169.50	172.00	162.90	164.00
17	193.68	193.89	192.79	193.62	181.60	183.67	179.90	180.80
18	209.94	210.10	208.30	208.92	196.50	197.21	195.62	196.23

Table A8: Max and min frequencies for removed bolts.

Mode	B1		B2		B3	
	5%	95%	5%	95%	5%	95%
1	6.60	6.62	4.68	4.70	5.43	5.43
2	8.61	8.62	8.29	8.30	6.31	6.31
3	8.80	8.82	8.80	8.83	8.81	8.83
4	26.47	26.50	26.46	26.50	26.37	26.46
5	43.81	43.85	43.43	43.47	43.79	43.83
6	47.23	47.27	44.05	44.06	44.39	44.41
7	53.80	53.86	52.42	52.46	46.63	46.64
8	61.56	61.58	61.55	61.58	61.52	61.54
9	80.29	80.32	80.26	80.29	80.23	80.25
10	97.55	97.57	97.53	97.55	97.52	97.54
11	115.92	115.95	115.86	115.90	115.74	115.76
12	131.95	132.07	128.74	128.89	127.81	128.77
13	137.02	137.07	135.21	135.29	131.74	131.98
14	145.26	145.40	142.74	142.85	136.66	136.74
15	156.15	156.18	156.07	156.14	155.90	155.96
16	177.23	177.29	177.17	177.29	177.05	177.09
17	194.77	194.83	194.70	194.78	194.60	194.67
18	211.16	211.36	211.13	211.33	209.47	209.83

Table A9: Max and min frequencies for cuts.

Mode	C1		C10		C20		C40	
	5%	95%	5%	95%	5%	95%	5%	95%
1	8.01	8.03	8.02	8.03	8.01	8.03	8.02	8.02
2	8.80	8.81	8.79	8.82	8.79	8.81	8.77	8.78
3	9.07	9.08	9.05	9.06	9.02	9.03	8.91	8.91
4	26.46	26.48	26.43	26.48	26.39	26.47	26.39	26.47
5	43.79	43.84	43.80	43.82	43.76	43.79	43.66	43.70
6	51.39	51.41	51.39	51.41	51.38	51.39	51.38	51.39
7	55.98	56.02	55.92	55.94	55.79	55.80	55.24	55.25
8	61.59	61.61	61.55	61.57	61.51	61.53	61.25	61.32
9	80.19	80.24	80.19	80.22	80.18	80.22	80.16	80.20
10	97.52	97.58	97.49	97.53	97.45	97.48	97.25	97.32
11	116.00	116.07	116.02	116.05	115.89	115.92	115.52	115.55
12	133.41	133.49	133.41	133.48	133.34	133.39	133.26	133.33
13	142.32	142.37	142.32	142.37	142.29	142.35	142.28	142.32
14	149.82	149.94	149.56	149.66	148.99	149.04	146.75	146.81
15	156.32	156.38	156.28	156.32	156.14	156.20	155.78	155.82
16	177.14	177.19	177.08	177.14	176.94	176.99	176.41	176.45
17	194.65	194.72	194.61	194.67	194.52	194.61	194.38	194.44
18	211.19	211.31	211.23	211.38	211.04	211.24	210.91	211.16

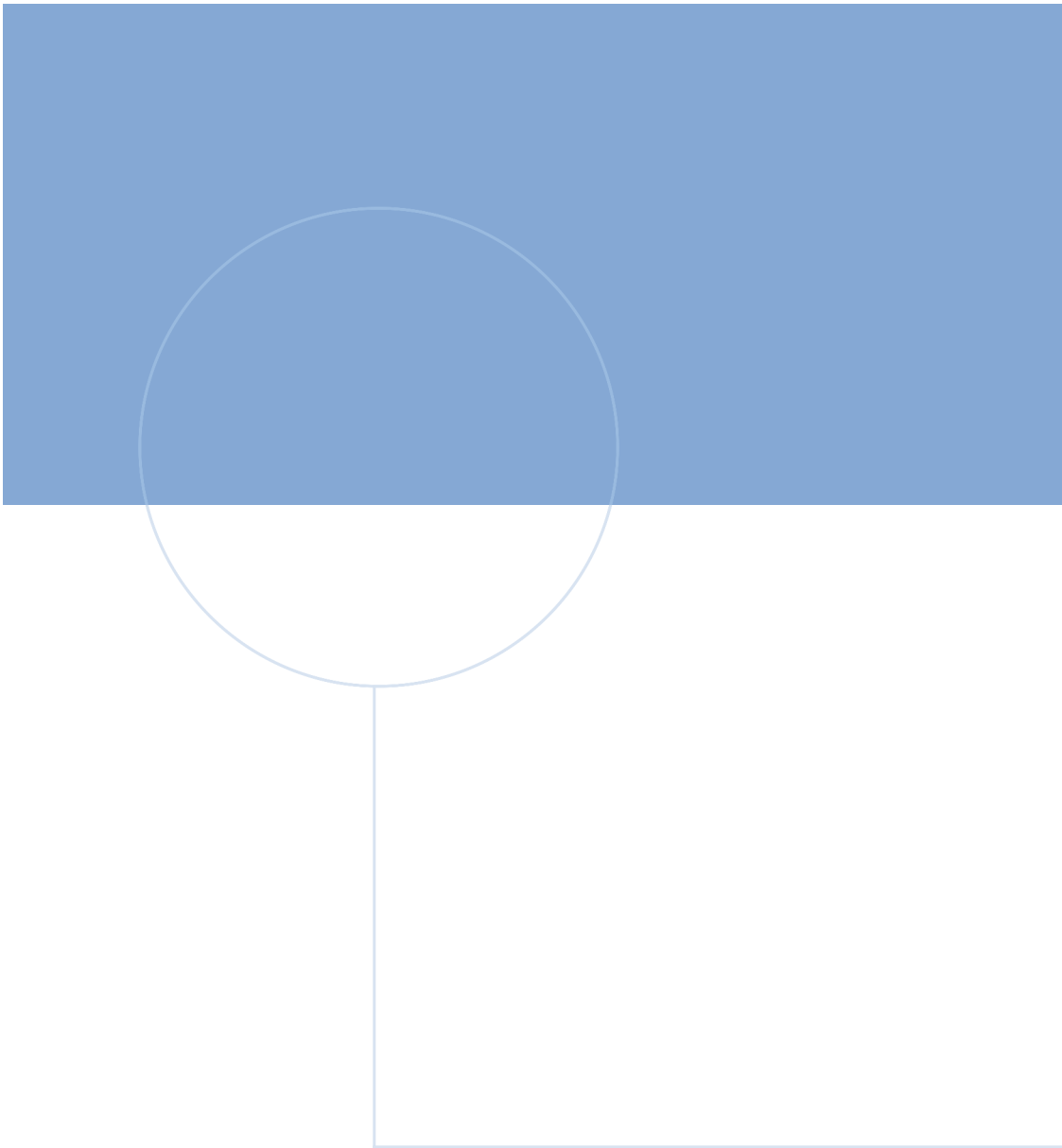

NTNU

Kunnskap for en bedre verden